GASP XXVII: Gas-phase Metallicity Scaling Relations in Disk Galaxies with and without Ram Pressure Stripping

Andrea Franchetto[1,2] ![ORCID], Benedetta Vulcani[2] ![ORCID], Bianca M. Poggianti[2] ![ORCID], Marco Gullieuszik[2] ![ORCID], Matilde Mingozzi[2] ![ORCID],
Alessia Moretti[2] ![ORCID], Neven Tomičić[2] ![ORCID], Jacopo Fritz[3] ![ORCID], Daniela Bettoni[2] ![ORCID], and Yara L. Jaffé[4] ![ORCID]

[1] Dipartimento di Fisica e Astronomia "Galileo Galilei," Università di Padova, vicolo dell'Osservatorio 3, I-35122, Padova, Italy; andrea.franchetto@phd.unipd.it
[2] INAF—Astronomical Observatory of Padova, vicolo dell'Osservatorio 5, I-35122 Padova, Italy
[3] Instituto de Radioastronomía y Astrofísica, UNAM, Campus Morelia, A.P. 3-72, C.P. 58089, Mexico
[4] Instituto de Fisica y Astronomia, Universidad de Valparaiso, Avda. Gran Bretana 1111 Valparaiso, Chile

Received 2019 November 29; revised 2020 April 21; accepted 2020 April 22; published 2020 June 2

Abstract

Exploiting the data from the GAs Stripping Phenomena in galaxies with MUSE (GASP) survey, we study the gas-phase metallicity scaling relations of a sample of 29 cluster galaxies undergoing ram pressure stripping and of a reference sample of (16 cluster and 16 field) galaxies with no significant signs of gas disturbance. We adopt the PYQZ code to infer the mean gas metallicity at the effective radius and achieve a well-defined mass–metallicity relation (MZR) in the stellar mass range $10^{9.25} \leqslant M_\star \leqslant 10^{11.5} \, M_\odot$ with a scatter of 0.12 dex. At any given mass, reference cluster and stripping galaxies have similar metallicities, while the field galaxies with $M_\star < 10^{10.25} \, M_\odot$ show on average lower gas metallicity than galaxies in clusters. Our results indicate that at the effective radius, the chemical properties of the stripping galaxies are independent of the ram pressure stripping mechanism. Nonetheless, at the lowest masses, we detect four stripping galaxies well above the common MZR that suggest a more complex scenario. Overall, we find signs of an anticorrelation between the metallicity and both the star formation rate and the galaxy size, in agreement with previous studies. No significant trends are instead found with the halo mass, clustercentric distance, and local galaxy density in clusters. In conclusion, we advise a more detailed analysis of the spatially resolved gas metallicity maps of the galaxies, able to highlight effects of gas redistribution inside the disk due to ram pressure stripping.

Unified Astronomy Thesaurus concepts: Galaxies (573); Field galaxies (533); Galaxy clusters (584); Metallicity (1031); Galaxy chemical evolution (580)

Supporting material: machine-readable table

1. Introduction

The gas-phase metallicity is known to show a well-established relation with the galaxy stellar mass in the range of 10^6 to $10^{12} \, M_\odot$ (Tremonti et al. 2004; Kewley & Ellison 2008; Mannucci et al. 2010; Sánchez et al. 2013, 2019; Barrera-Ballesteros et al. 2017; Hirschauer et al. 2018; Blanc et al. 2019). Decades of studies proposed several interpretations for this correlation invoking outflows of enriched gas driven by stellar/active galactic nuclei (AGNs) feedback (e.g., Garnett 2002; De Rossi et al. 2017; Chisholm et al. 2018), infall of pristine gas (Mannucci et al. 2010), evolutionary stage and downsizing (high-mass galaxies evolve more rapidly than low-mass galaxies, becoming metal-rich at earlier epochs; Maiolino et al. 2008), and dependence of the initial mass function (IMF) on galaxy mass with changes of the stellar yields (De Masi et al. 2018). However, the shape of the mass–metallicity relation (MZR) could stem from the combination of all these processes (Maiolino & Mannucci 2019). Recent studies at low and intermediate redshift investigated the role of several parameters to explain the scatter around the relation and discern between the mechanisms that are shaping the relation.

In the last decade, attention turned to the role of star formation rate (SFR) in explaining the scatter along the MZR. Using a sample of $\sim$40,000 SDSS star-forming galaxies, Ellison et al. (2008) was the first to find an anticorrelation between the gas-phase metallicity and the specific SFR (sSFR, SFR per unit of galaxy stellar mass) at a given mass. The existence of a well-defined relation between the stellar mass, gas-phase metallicity, and SFR was discussed in detail by Mannucci et al. (2010),

exploiting a sample of $\sim$140,000 star-forming galaxies from SDSS. The analytic form of their so-called fundamental metallicity relation (FMR) describes a surface in 3D space of the parameters involved, and the scatter in metallicity along this surface is reduced with respect to that observed for the MZR (see also Lara-López et al. 2010; Hunt et al. 2012; Yates et al. 2012). The explanation of the FMR invokes metal-poor gas accretion that, on one hand, implicates metal dilution and, on the other hand, produces star formation activity (Mannucci et al. 2010). Integral-field unit data seem to be still consistent with the mass–SFR–metallicity relation (Cresci et al. 2019), even if the results are largely debated and some authors find a weak or no secondary dependence on SFR (Sánchez et al. 2013, 2017, 2019; Barrera-Ballesteros et al. 2017).

Ellison et al. (2008) also explored the connection between the stellar mass, the gas-phase metallicity, and the galaxy size and found that compact galaxies exhibit higher metallicity than larger ones. Sánchez Almeida & Dalla Vecchia (2018) investigated this relation using the EAGLE cosmological numerical simulation and discovered similar results. Their analysis shows that the anticorrelation between the gas-phase metallicity and the galaxy size is due to the late gas accretion. Galaxies grow in size with time, so if they experience recent metal-poor infall of gas, they will be bigger and with lower gas-phase metallicity than those formed earlier.

Many studies also show that the environment may play a role in shaping the MZR and that the overdense environment, where many specific mechanisms can affect the gas reservoir, can

alter the gas-phase metallicity (e.g., Cooper et al. 2008; Ellison et al. 2009; Peng & Maiolino 2014; Wu et al. 2017; Maier et al. 2019a, 2019b). For example, Ellison et al. (2009) studied a sample of ∼1300 cluster galaxies and reported that on average they have an overabundance of gas-phase metallicity up to 0.05 dex in comparison with a control sample of galaxies that are not cluster members. However, their study ascribes this effect to the local galaxy density and not to the cluster membership, as control galaxies at locally high densities exhibit metal enhancements similar to the cluster ones. In addition, for the massive cluster galaxies, the overabundance resulted independently of the global cluster properties (e.g., virial radius, halo mass). Peng & Maiolino (2014) analyzed ∼16,000 satellite galaxies and observed a strong correlation between the gas metallicity and the overdensity at a given mass, proposing metal-enriched inflows in crowded environments as explanation. Pilyugin et al. (2017), using a sample of ∼77,600 late-type galaxies, found that mainly low-mass galaxies ($10^{9.1} < M_\star < 10^{9.6}\ M_\odot$) show on average an excess of gas metallicity in the densest environments, but a large scatter is observed at any density of the environment. The dependence on the environment could be explained in terms of gas content. In fact, the metallicity anticorrelates with the SFR and the gas fraction, which in turn appear to be both anticorrelated with the local density (Wu et al. 2017). Maier et al. (2019a, 2019b) found an enhancement of oxygen abundance for galaxies inside the virialized region of clusters and argued for the importance of environmental processes such as strangulation (halo gas removal by the intracluster medium—ICM—interaction; Larson et al. 1980).

All of the aforementioned studies have therefore highlighted the connection between SFR, galaxy size, and environment with the gas content of the galaxies, and simulations indeed find a strong relation between the gas-phase metallicity and the gas fraction of galaxies (De Rossi et al. 2016, 2017). In the context of galaxy evolution, testing the metallicity scaling relations provides an important tool to study the many physical processes in galaxies and, in particular, the effects due to the mechanisms affecting the gas reservoir. A gas deficit is often observed in cluster galaxies due to different environmental processes (Boselli & Gavazzi 2006): thermal evaporation (Cowie & Songaila 1977), starvation (Larson et al. 1980), and ram pressure stripping (RPS; Gunn et al. 1972). RPS due to the interaction between the ICM and the interstellar medium (ISM) is one of the most efficient gas removal processes from galaxies in clusters. Indeed, the study of the gas-phase metallicity in galaxies undergoing this process could provide constraints on the gas redistribution inside the galaxy disk.

In this paper, we indeed explore the gas metallicity scaling relations of a sample of galaxies undergoing RPS, exploiting the Gas Stripping Phenomena in galaxies with MUSE (GASP; Poggianti et al. 2017b) data. GASP is an ESO Large Program carried out with the integral-field spectrograph MUSE (Bacon et al. 2010) mounted on the VLT (Paranal) aiming at systematically studying the gas removal processes from galaxies in different environments. MUSE allows the spatially resolved distribution of the ionized gas emission to be explored in detail not only within the galaxy disk but also along the gas stripped beyond the stellar extent.

So far, the gas-phase metallicity has only been derived for a limited number of extreme RPS galaxies (e.g., Fossati et al. 2016; Bellhouse et al. 2017, 2019; Gullieuszik et al. 2017; Poggianti et al. 2017b; Moretti et al. 2018). In this work, we instead analyze this quantity for the first time in a statistically meaningful sample and compare the properties of RPS galaxies to those of a sample of undisturbed galaxies in clusters and the field from the same survey.

In Section 2, we present the galaxy sample extracted from the GASP data. Section 3 describes the methods adopted to measure the main properties of the galaxies. The MZRs of the sample are shown and analyzed in Section 4, while the interconnection between the gas-phase metallicity and other parameters is explored in detail in Section 5. In Section 6, we conclude with a summary of our work.

This paper is the first of a series focusing on the statistical study of the chemical properties of the ionized gas component in galaxies experiencing RPS.

This paper adopts a Chabrier (2003) initial mass function (IMF) and standard concordance cosmology parameters $H_0 = 70$ km s^{-1} Mpc^{-1}, $\Omega_M = 0.3$, and $\Omega_\Lambda = 0.7$.

2. Sample and Observations

The GASP project observed 114 disk galaxies at $0.04 < z < 0.07$ in different environments (galaxy clusters, groups, filaments, and isolated) and with stellar mass in the range $10^{8.7} < M_\star < 10^{11.5}\ M_\odot$. The sample includes 76 galaxies in clusters taken from the WINGS (Fasano et al. 2006) and OMEGAWINGS (Gullieuszik et al. 2015) cluster surveys and 38 galaxies in less massive environments taken from the PM2GC catalog (Calvi et al. 2011). The GASP targets and the observing strategy are described in detail in Poggianti et al. (2017b).

The final data cubes consist of 300×300 spaxels with a spatial sampling of $0\rlap{.}''2 \times 0\rlap{.}''2$. We stress that for all GASP galaxies, the field of view (FoV) of MUSE is able to cover from 3 to 15 effective radii (R_e) from their center, with a mean of $7\,R_e$. This coverage allows us to observe the full optical extent of the galaxies and includes a wide portion of sky around them.

2.1. Selection of the Sample

We extract from the GASP sample the cluster galaxies showing unilateral ionized gas beyond their stellar disk (from a few kiloparsecs to 100 kpc), while having the old stellar component (formed more than 6×10^8 yr ago) morphologically undisturbed. These signs indicate galaxies are suffering from ram pressure by the ICM. We include galaxies at different stripping stages (from initial stripping with a lopsided distribution of the gas component to extreme stripping galaxies with tens of kiloparsecs gas tails) and exclude truncated disk galaxies (galaxies with gas disk less extended than the stellar one and with no ionized gas tails). This selection yields 29 galaxies that we will call the "stripping" sample.

From the GASP sample, we also draw a sample of galaxies that will constitute a "reference" sample. These galaxies, located both in clusters and in the less dense environments (field and groups), do not exhibit clear signs of ongoing gas-stripping processes (no evident gas tails or gas debris well beyond the stellar disk) and have regular ionized gas and stellar distributions. Nonetheless, we note that these galaxies might still be partially affected by some physical processes that we are not able to identify.[5]

---

[5] We have, however, removed from the sample peculiar galaxies showing signs of tidal interactions, galaxies with a companion, and field galaxies with clear signs of specific processes in action (Vulcani et al. 2018a, 2018c, 2019).

The reference sample includes 16 cluster galaxies and 16 galaxies in less dense environments, defined as the "reference cluster" and "reference field" sample, respectively. The complete list of galaxies included in the analysis will be given in Table 1.

Figure 1 shows the stellar mass distributions of the different samples. The stripping galaxies span a wide range in stellar mass, going from $10^{8.7}$ to $10^{11.5}\,M_\odot$. Reference cluster galaxy masses range from $10^{9.2}$ to $10^{10.5}\,M_\odot$, while reference field galaxy masses reach $10^{11}\,M_\odot$. The mass ranges of the total reference sample (cluster+field) and the stripping sample overlap for about two orders of magnitude, even though, according to the Kolmogorov–Smirnov (KS) test, their mass distributions are drawn from different parent distributions (p-value <5%).

Regarding the mass of the host environment, galaxies in the reference field sample belong to a low-mass dark matter halo ($11.2 < \log M_{\mathrm{halo}}/M_\odot < 12.9$) with at most five members. Instead, the masses of the clusters, in which the stripping and the reference cluster galaxies live, span a range of $13.8 < \log M_{\mathrm{halo}}/M_\odot < 15.4$.[6]

Considering only cluster galaxies, Figure 2 shows the projected phase-space diagram for stripping and reference galaxies. This diagram compares the line-of-sight velocity of each galaxy with respect to the cluster mean velocity $|\Delta v|$, normalized by the cluster velocity dispersion σ_{cl} against its projected clustercentric distance r_{p} normalized by the cluster virial radius R_{200} (σ_{cl} and R_{200} are taken from Gullieuszik et al. 2020). The phase-space diagram allows us to study galaxy properties as a function of the orbital histories of the galaxies within the clusters. As shown in Jaffé et al. (2018), the stripping efficiency increases as galaxies move toward higher velocities and lower distances from the cluster cores. Galaxies of the two samples occupy different regions of the diagram. Twenty-four stripping galaxies (83% of the stripping sample) are within $1\,R_{200}$, while the reference cluster galaxies are all located beyond $0.7\,R_{200}$. Although both samples show a large velocity scatter, the stripping sample has a higher mean value ($\langle|\Delta v|/\sigma_{\mathrm{cl}}\rangle = 1.35$) than the reference cluster one ($\langle|\Delta v|/\sigma_{\mathrm{cl}}\rangle = 0.76$). The two-dimensional KS test states with high confidence that the two samples are not drawn from the same parent distribution (p-value < 0.0004). In Section 5, we explore the impact of this difference on the gas-phase metallicity of the sample galaxies.

3. Data Analysis

The methods employed in the analysis of the MUSE data cubes are explained in detail in Poggianti et al. (2017b). Briefly, data were reduced with the most updated version of the MUSE pipeline at the moment of observations (Bacon et al. 2010)[7] and corrected for extinction due to our own Galaxy assuming the extinction law from Cardelli et al. (1989). The data cubes were average filtered in the spatial direction with a 5×5 pixel kernel, corresponding to $1'' = 0.7$–$1.3\,\mathrm{kpc}$, depending on the galaxy redshift.

Each spectrum is corrected for the underlying stellar absorption subtracting the stellar-only component derived with our spectrophotometric code SINOPSIS (Fritz et al. 2017). The emission-line fluxes with the associated errors are measured by

the IDL software KUBEVIZ (Fossati et al. 2016) that employs Gaussian profile fitting. The emission lines of interest for this work are Hβ, [O III]5007, [O I]6300, Hα, [N II]6583, [S II]6716, and [S II]6731. We adopt the Cardelli et al. (1989) extinction law to correct the emission-line fluxes for extinction by dust internal to the galaxy considering the observed Balmer decrement and assuming an intrinsic Hα/Hβ ratio of 2.86.

In addition, SINOPSIS delivers several spatially resolved properties of the stellar component. In this paper, we make use of the stellar masses and calculate the total stellar mass of each galaxy, by summing the values of all spaxels belonging to the galaxy disk, as in Vulcani et al. (2018b). The definition of the galaxy boundary is developed by Gullieuszik et al. (2020) and already exploited by Vulcani et al. (2018b) and Poggianti et al. (2019).

We use the diagnostic BPT diagram (Baldwin et al. 1981) [O III]5007/Hβ versus [N II]6583/Hα to divide the regions dominated by star formation (SF), Composite (SF+AGN), AGN, and LI(N)ERs (low-ionization nuclear emission regions). We use the separation lines from Kauffmann et al. (2003), Kewley et al. (2001), and Sharp & Bland-Hawthorn (2010). We note that some of the most massive galaxies in the stripping sample host either an AGN or LINERs, while no galaxy of the reference sample does. A detailed analysis of the AGN in these galaxies is presented in Radovich et al. (2019).

3.1. Structural Parameters

The structural parameters of each galaxy are derived from the analysis of the I-band images obtained from the integrated MUSE data cubes using the Cousins I-band filter response curve. In the Appendix, we describe in detail the surface brightness analysis carried out to derive all the quantities. Briefly, we use the ELLIPSE task in IRAF to derive the isophotal segmentation of the galaxies (Jedrzejewski 1987). The extraneous sources and bright spots are masked out to achieve a smooth luminosity distribution of the galaxy. The ELLIPSE algorithm fits the galaxy isophotes with a series of ellipses to minimize the deviations from the true shape of the isophotes. It then returns the values of the semimajor axes, surface brightness, position angle (PA), and ellipticity (ε) of each elliptical isophote. We calculate the luminosity growth curve $L(R)$ of the galaxies by trapezoidal integration of their surface brightness profiles. By definition, the effective radius (R_{e}) is the radius such as $L(R_{\mathrm{e}})/L_{\mathrm{tot}} = 0.5$. We set L_{tot} as the total luminosity within the most external fitted isophote, ensuring that it encloses entirely the full optical extent of the galaxy (see the Appendix). We derived the ε and PA of the disk as the average values of the elliptical isophotes corresponding to the galaxy disk. The galaxy inclination i is computed as

$$\cos^2 i = \frac{(1 - \varepsilon)^2 - q_0^2}{1 - q_0^2}, \qquad (1)$$

where we assume an intrinsic flattening for galaxies of $q_0 = 0.13$ (Giovanelli et al. 1994).

Note that two stripping galaxies (JO149 and JO95) have an irregular I-band morphology that prevents a good estimate of their structural parameters. Therefore, we fix their ε to zero and estimate their R_{e} using the mass–size relation of Equation (A3) in the Appendix for the stripping galaxies.

With the quantities just described, we deproject the position of each spaxel to derive its physical galactocentric distance. We

---

Table 1
Properties of the Sample

ID	Sample	Redshift	$\log(M_\star/M_\odot)$ (dex)	$R_{\rm e}$ (arcsec)	i (deg)	PA (deg)	$\left\langle\frac{\rm O}{\rm H}\right\rangle_{<0.1\,R_{\rm e}}$ (dex)	$\left\langle\frac{\rm O}{\rm H}\right\rangle_{<0.5\,R_{\rm e}}$ (dex)	$\left\langle\frac{\rm O}{\rm H}\right\rangle_{@\,R_{\rm e}}$ (dex)	$\left\langle\frac{\rm O}{\rm H}\right\rangle_{\rm disk}$ (dex)	$\left\langle\frac{\rm O}{\rm H}\right\rangle_{@\,R_{\rm e}}$ CU17 (dex)
JO73	RF	0.0713	10.03 ± 0.10	$4.24^{+0.25}_{-0.27}$	33 ± 1	75 ± 2	8.98 ± 0.01	8.86 ± 0.08	8.59 ± 0.06	8.56 ± 0.13	8.59 ± 0.05
P13384	RF	0.0512	9.85 ± 0.11	$3.37^{+0.29}_{-0.28}$	29 ± 8	171 ± 38	8.82 ± 0.00	8.76 ± 0.04	8.56 ± 0.04	8.53 ± 0.09	8.56 ± 0.05
JO68	RC	0.0579	9.99 ± 0.09	$4.40^{+0.25}_{-0.28}$	56 ± 1	66 ± 2	9.04 ± 0.02	8.97 ± 0.04	8.83 ± 0.05	8.79 ± 0.09	8.69 ± 0.02
JO89	RC	0.0419	9.73 ± 0.08	$6.41^{+0.57}_{-0.61}$	66 ± 1	80 ± 2	8.83 ± 0.02	8.79 ± 0.06	8.70 ± 0.11	8.69 ± 0.12	8.65 ± 0.04
JO113	S	0.0595	9.69 ± 0.09	$3.53^{+0.19}_{-0.23}$	73 ± 1	22 ± 1	8.76 ± 0.00	8.74 ± 0.02	8.61 ± 0.06	8.52 ± 0.10	8.58 ± 0.05
JO135	S	0.0554	10.99 ± 0.07	$4.61^{+0.15}_{-0.17}$	64 ± 2	43 ± 1	$\cdots$	$\cdots$	$\cdots$	8.98 ± 0.09	$\cdots$

Note. Columns are (1) GASP ID number, (2) sample (RF is reference field, RC is reference cluster, S is stripping), (3) galaxy redshift (for field galaxies) or mean galaxy cluster redshift (for cluster galaxies), (4) logarithm of the galaxy stellar mass, (5) $R_{\rm e}$, (6) disk inclination, (7) PA measured counterclockwise from the north direction, (8)–(11) mean gas-phase metallicity within 0.1 $R_{\rm e}$, within 0.5 $R_{\rm e}$, at $R_{\rm e}$ and beyond 0.5 $R_{\rm e}$, respectively, using PYQZ, and (12) mean gas-phase metallicity at $R_{\rm e}$ using the O3N2 calibration of Curti et al. (2017).

(This table is available in its entirety in machine-readable form.)
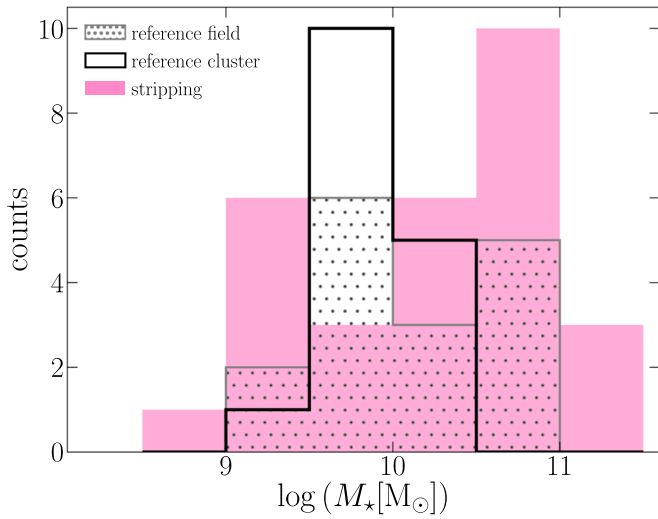
Figure 1. Galaxy stellar mass distribution of the reference field (dotted gray histogram), reference cluster (solid black histogram), and stripping (pink histogram) samples.
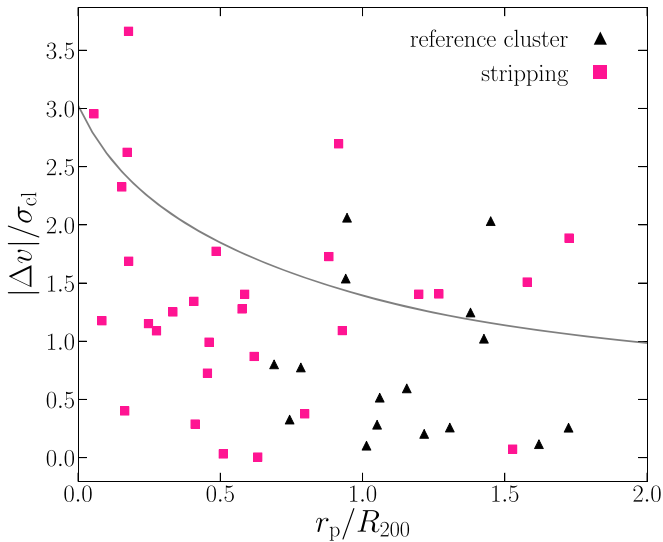

Figure 2. Projected velocity vs. projected position phase-space diagram of the reference cluster galaxies (black triangles) and the stripping galaxies (pink squares). The curve shows the escape velocity in a Navarro et al. (1996) halo assuming a concentration value of 6.

do not apply the deprojection procedure for galaxies with low inclination ($i < 35°$), because the correction effect could be smaller than the uncertainties that the deprojection could introduce.

The structural parameters for all our galaxies are listed in Table 1.

3.2. Gas-phase Metallicity

We compute the gas-phase metallicity, here referring to the oxygen abundance, separately adopting two different metallicity calibrators, the PYQZ code (Dopita et al. 2013; Vogt et al. 2015), and the Curti et al. (2017) empirical calibrator based on the O3N2 indicator, to explore their impact on the results.

We use a modified version of PYQZ v0.8.2 (F. Vogt 20217, private communication) that relies on a set of line-ratio grids computed with MAPPINGS IV (Sutherland & Dopita 1993; Dopita et al. 2013). This version is tested in the range

$7.39 \leqslant 12 + \log(O/H) \leqslant 9.39$ and adopts the solar oxygen abundance $12 + \log(O/H)_{\odot} = 8.69$. The code simultaneously estimates the gas-phase metallicity $12 + \log(O/H)$ and the ionization parameter[8] $\log q$, given a set of emission-line ratios. To compute the gas-phase metallicity from the spectra, we consider the model grid projected on the line-ratio plane [O III]$\lambda5007$/[S II]$\lambda\lambda6717,6731$ versus [N II]$\lambda6583$/[S II]$\lambda\lambda6717,6731$, which, as demonstrated in Dopita et al. (2013), does not present degeneration between the gas metallicity and the ionization parameter and allows an excellent separation of these quantities in the tested range of values. Given the pair of line ratios required by the adopted grid, PYQZ returns a determined pair of $12 + \log(O/H)$ and $\log(q)$. Because the photoionization models cannot fully reproduce all observed line ratios, their predicted fluxes present an uncertainty of $\sim$0.1 dex (Kewley & Ellison 2008; Dopita et al. 2013; Blanc et al. 2015; Mingozzi et al. 2020). In order to investigate the effect of this uncertainty on the gas metallicity error, we select 81 line-ratio pairs homogeneously covering the model grid used by our PYQZ version. For each of the 81 original points, we create a subset of 1000 line-ratio values randomly distributed around the original point in a normal distribution with a sigma of 0.1 dex. Using PYQZ, we translate each subset in a gas metallicity distribution, and we calculate their dispersion, which corresponds to the systematic error associated with the gas metallicity of the original point. To summarize, we find that an uncertainty of 0.1 dex on the models is translated into a systematic error on the metallicity estimate of $\sim$0.05 dex for the highest metallicities (i.e., $12 + \log(O/H) = 9.39$), up to 0.3 dex for the lowest metallicities (i.e., $12 + \log(O/H) = 7.39$). In our sample, most oxygen abundances are above 8.0, for which the aforementioned systematic uncertainty is smaller than 0.15 dex. Overall, this systematic error is usually dominant with respect to the uncertainty introduced by the errors on the emission-line flux measurements.

The calibration of Curti et al. (2017) is based on the indicator O3N2, defined as

$$O3N2 = \log\left(\frac{[O\ III]5007}{H\beta}\right) - \log\left(\frac{[N\ II]6583}{H\alpha}\right), \qquad (2)$$

which is inversely proportional to the oxygen abundance. It is obtained on stacked spectra of local galaxies in the SDSS-DR7 (Equation (5) with parameter values in Table 2 in Curti et al. 2017). Their galaxies have a scatter of 0.21 dex with respect to the derived calibration, with a mean dispersion along the metallicity direction of 0.09 dex. The inferred metallicities are normalized to the solar value $12 + \log(O/H)_{\odot} = 8.69$ and the relation is tested within the range $7.6 \leqslant 12 + \log(O/H) \leqslant 8.85$.

We note that we are not taking into account the contamination of the diffuse ionized gas (DIG; see Haffner et al. 2009 for a complete review), and no separation criterion is adopted to exclude the spaxels dominated by the emission of this component, which in principle could have different line ratios (e.g., Zhang et al. 2017). The DIG properties and its spatial distribution will be indeed discussed in detail in N. Tomičić et al. (2020, in preparation).

---

[8] The ionization parameter is expressed as $q = Uc$, where U is the ratio between the density per unit volume of ionizing photons and the gas particle number density, and c is the speed of light.

We measure the gas-phase metallicity in each spaxel whose ionized gas flux is powered by SF, requiring a signal-to-noise ratio (S/N) $\geqslant 3$ for all the involved emission lines.[9]

3.3. Gas Metallicity Average of the Galaxies

Thanks to the wide FoV of MUSE (see Section 2), we can sample the whole extension of the ionized gas that, excluding the gas tails, reaches a median of $\sim 3\,R_e$ (Vulcani et al. 2019). Taking into account only the star-forming spaxels for which we can infer the gas metallicity, we are able to analyze the chemical properties of the gas up to $1.9\,R_e$ for all the reference galaxies, and beyond $2.5\,R_e$ for half of them. For the stripping galaxies, we can derive the gas-phase metallicity from the center to the gas tails, but in this work, we limit our analysis only to the gas within the galaxy stellar disk.

To choose a suitable representative gas-phase metallicity of the galaxy, we explore four possible definitions by computing the mean oxygen abundance of the star-forming spaxels in four different radial ranges:

$\langle \mathrm{O/H} \rangle_{< 0.1\,R_e}$: spaxels within $0.1\,R_e$;

$\langle \mathrm{O/H} \rangle_{< 0.5\,R_e}$: spaxels within $0.5\,R_e$;

$\langle \mathrm{O/H} \rangle_{@\,R_e}$: spaxels in the range $0.95\text{–}1.05\,R_e$;

$\langle \mathrm{O/H} \rangle_{\mathrm{disk}}$: spaxels beyond $0.5\,R_e$ and within the galaxy disk, assuming the same galaxy boundary adopted to derive the total stellar mass.

We decide to exploit the spatially resolved data and not to infer the metallicity from integrated spectra inside the radial ranges of interest to avoid summing together spaxel spectra that in principle have different physical properties (e.g., gas metallicity, ionization parameter, SFR), and thus different emission-line ratios. The use of an integrated spectrum entails a luminosity-weighted mean metallicity, while we aim at estimating the average metallicity assigning the same weight to every spaxel. In addition, as discussed by Sanders et al. (2017), gas-phase metallicities derived from global galaxy spectra will be systematically biased by the effects of flux weighting of multiple H II regions.

For some galaxies, the number of available spaxels is quite low, either given the paucity of ionized gas, or due to the presence of regions not powered by stellar photoionization or due to spaxels with S/N < 3. To ensure a suitable statistics to calculate the global metallicity, we require that either more than one-third of the spaxels, or at least 150 spaxels within the considered radial range, have measured oxygen abundance values. If neither condition is fulfilled in the computation of the mean metallicity, the value is discarded.

The uncertainty that we associate with the mean metallicity corresponds to the standard deviation of the star-forming spaxel metallicities considered in each radial range. For the sake of clarity, we do not include the additional error due to the systematic error of the calibration. We note that this must be divided by the root of the number of valid spaxels in the radial bin of interest, giving a contribution to the error budget lower than 0.02 dex.

---

[9] Mannucci et al. (2010) reported that applying a high S/N threshold to the involved emission lines might bias the metallicity measurements. In fact, at the lowest metallicities, the flux of the [N II]6583 line becomes faint and some spaxels might be removed, shifting high the measured metallicity. Nonetheless, checking the S/N distribution in our galaxies, we find that only the most external spaxels might be affected, but these will be disregarded in the following analysis anyway.

The metallicity estimates for all our galaxies are listed in Table 1.

Seventeen galaxies do not fulfill the condition of the minimum number of spaxels with measured oxygen abundance to estimate the $\langle \mathrm{O/H} \rangle_{< 0.1\,R_e}$, as they have AGNs, LINERs, and central composite regions or central gas holes. For 10 of them, we also cannot derive $\langle \mathrm{O/H} \rangle_{< 0.5\,R_e}$ for the same reason, and for the remaining 7, the $\langle \mathrm{O/H} \rangle_{< 0.5\,R_e}$ measure might be underestimated due to the absence of the innermost spaxels that presumably could have higher metallicity. Instead, the $\langle \mathrm{O/H} \rangle_{@\,R_e}$ and $\langle \mathrm{O/H} \rangle_{\mathrm{disk}}$ measurements for these galaxies are independent of the presence of a central LINER or AGN, as central pixels are not considered in their computation, by definition. Moreover, adopting the Kauffmann et al. (2003) separation line to select the star-forming spaxels, instead of the less restrictive separation proposed by Kewley et al. (2001), we make sure to include in the analysis only the spectra with the least or no AGN/LINER contamination. However, the $\langle \mathrm{O/H} \rangle_{@\,R_e}$ and $\langle \mathrm{O/H} \rangle_{\mathrm{disk}}$ quantities could still suffer from the possible absence of pixels not powered by stellar photoionization or lacking gas along the disk.

We can estimate the $\langle \mathrm{O/H} \rangle_{@\,R_e}$ and $\langle \mathrm{O/H} \rangle_{\mathrm{disk}}$ for all galaxies except JO135 and JW100, which do not satisfy the minimum number of required spaxels to compute the $\langle \mathrm{O/H} \rangle_{@\,R_e}$ the former when using both calibrators and the latter when using that based on the O3N2 index.

Finally, we report that selecting the star-forming spaxels according to the O I-based BPT diagram [O III]5007/Hβ versus [O I]6300/Hα, instead of the N II-based BPT diagram, does not influence the inferred global galaxy metallicities. The differences between the oxygen abundance at R_e derived using the O I and the N II diagrams are at the $<0.1\sigma$ level on average using both calibrators. For this reason, in what follows we only show the results based on the star-forming spaxels selected with the N II-based BPT diagram.

3.4. Comparison of the Gas Metallicities

In this section, we first compare the values of gas-phase metallicity obtained using the radial ranges defined above, with the aim to understand which definition is the most suitable for our analysis and then the values of gas-phase metallicity obtained using the different calibrators.

In Figure 3, we compare the four definitions of galaxy gas-phase metallicity inferred with PYQZ. In each panel, we only plot the galaxies that fulfill the minimum number of required spaxels in the metallicity measurement. The tightest correlation occurs between $\langle \mathrm{O/H} \rangle_{< 0.1\,R_e}$ and $\langle \mathrm{O/H} \rangle_{< 0.5\,R_e}$ with an rms of 0.03 dex.

We remind the readers that the uncertainty associated with the mean metallicity is the standard deviation of the star-forming pixel metallicities within the considered radial range.

The $\langle \mathrm{O/H} \rangle_{< 0.1\,R_e}$ shows the smallest uncertainties because the central pixels have almost the same metallicity. Instead, the $\langle \mathrm{O/H} \rangle_{\mathrm{disk}}$ quantity has the largest uncertainties as the pixel gas metallicities inside the galaxy disk spread on a large range of values.

In the middle panels, we show the comparison of $\langle \mathrm{O/H} \rangle_{< 0.1\,R_e}$ (on the left), and $\langle \mathrm{O/H} \rangle_{< 0.5\,R_e}$ (on the right) with the oxygen abundance at R_e. $\langle \mathrm{O/H} \rangle_{@\,R_e}$ exhibits a well-defined correlation with both quantities, in particular with $\langle \mathrm{O/H} \rangle_{< 0.5\,R_e}$. The first two bottom panels depict the relations of the central
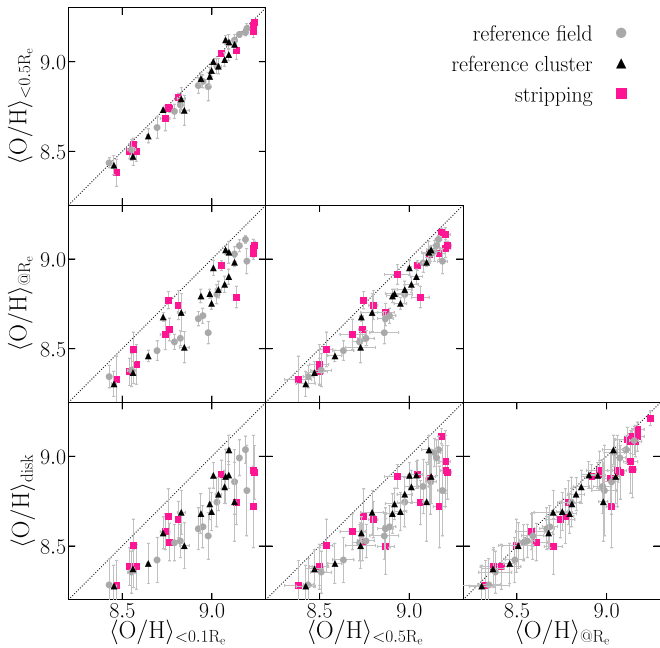
Figure 3. Comparison between the gas-phase metallicities inferred with PYQZ in different radial regions of the galaxies. The gray circles, black triangles, and pink squares indicate the reference field, reference cluster, and stripping galaxies, respectively. The black dotted lines are the 1:1 relations.

Figure 4. Comparison of the gas-phase metallicity at the R_e derived using the calibration proposed by Curti et al. (2017) and the calibration based on the PYQZ code. The symbols are as in Figure 3. The green line and the shaded area are the best linear fit of Equation (3) and the rms around the relation, respectively. The black dotted line is the 1:1 relation.

metallicities with $\langle O/H\rangle_{disk}$. We still observe a good correlation, although the scatter is slightly larger.

The bottom-right panel in Figure 3 illustrates the distribution of $\langle O/H\rangle_{disk}$ versus $\langle O/H\rangle_{@\,R_e}$. Both quantities show a tight correlation, with an rms of 0.07 dex, even if in the high-metallicity regime the spread becomes larger. The $\langle O/H\rangle_{@\,R_e}$ values exhibit smaller uncertainties than $\langle O/H\rangle_{disk}$ because the metallicity distribution of the pixels at R_e is narrower than that of the pixels along the whole disk. This is in agreement with the considerations of Sánchez et al. (2013, 2017), who compared the total gas-phase metallicity and that at R_e for hundreds of galaxies from the CALIFA survey using different calibrators, including PYQZ.

It is worth noting that $\langle O/H\rangle_{disk}$ especially could be affected by the stripping history of the stripping galaxies and the distribution of the regions not powered by stellar photoionization. In fact, $\langle O/H\rangle_{disk}$ could become less representative when the gas-phase metallicities of the excluded regions and that of the stripped gas highly differ from the regions included.

We repeat this analysis considering the oxygen abundance derived with the calibrator based on the O3N2 index. We obtain again a good correlation between the quantities and find that the conclusions discussed for the values derived with the PYQZ code are also valid for the O3N2 calibrator.

Because one of these methods is sufficient to describe the metallicity of these galaxies, we decide to adopt $\langle O/H\rangle_{@\,R_e}$ as the reference for the galaxy gas-phase metallicity, allowing us to characterize nearly all galaxies while avoiding the critical central regions.

We now focus our attention to the metallicity indicators. The choice of the metallicity calibration has a strong effect on the shape of the MZR, and systematic discrepancies are common between the results of the different measurement methods (Kewley & Ellison 2008). Figure 4 illustrates the comparison of the $\langle O/H\rangle_{@\,R_e}$ values derived with the calibration proposed by Curti et al. (2017) for the O3N2 index and the calibration
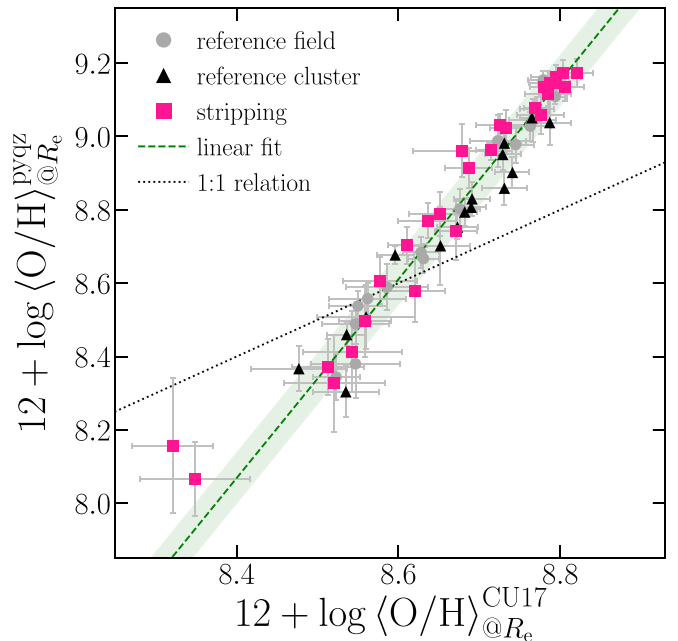
based on the PYQZ code. We fit the values with a linear relation weighted on the errors of both quantities. The best fit is

$$\langle Z\rangle_{pyqz} = (2.71 \pm 0.07)(\langle Z\rangle_{CU17} - 8.69) + (8.85 \pm 0.01), \quad (3)$$

where $\langle Z\rangle = 12 + \log\langle O/H\rangle_{@R_e}$.

The rms around the relation is 0.07 dex, and the Pearson correlation is $r[d.f = 57] = 0.98$ ($p \sim 0$). For the more metal-poor galaxies (JO149 and JO181), we observe the largest differences even though they are consistent with the linear relation within 1σ. We ascribe this offset to the strong dependence on the ionization parameter of the O3N2 index (see, e.g., Krühler et al. 2017; Rodríguez-Baras et al. 2019). For high ionization, the O3N2 is overestimated, driving the underestimation of the gas metallicity using the empirical relation of Curti et al. (2017), in particular for metal-poor gas. By a visual inspection of the spatially resolved distribution of the log q quantity, derived with the PYQZ code, we detect that the central regions of both galaxies are dominated by large ionization parameter values. Therefore, the metallicity of JO149 and JO181 obtained by the O3N2 calibrator could be biased toward lower values.

Overall, although the absolute values of the gas metallicity are different, the relative values remain reliable and the correlation is narrow, indicating that the metallicity distribution within the sample is independent of the choice of the calibrator.

In what follows, we show only the results obtained with the PYQZ calibration.

4. Results

4.1. Mass–Metallicity Relation

One of the aims of this work is to analyze the galaxy gas-phase metallicity versus the stellar mass diagram, illustrated in
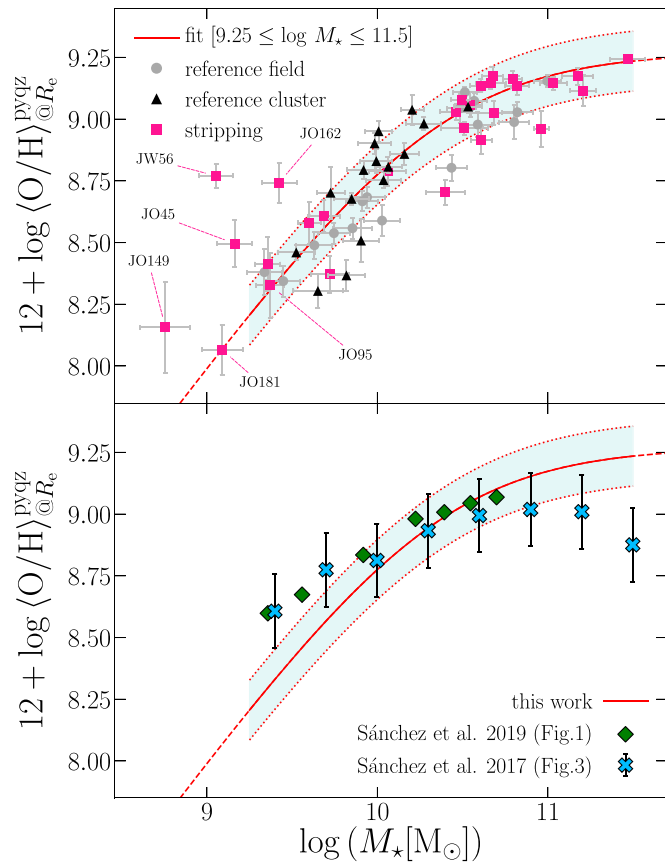
Figure 5. Upper panel: relation between the galaxy stellar mass and the PYQZ gas-phase metallicity at R_e. Symbols are as in Figure 3. The red line represents the best fit assuming Equation (4). The shaded area between the red dotted lines is the scatter around the fit. We comment on the flagged galaxies in the text. Bottom panel: comparison between the MZR derived in this work (red curve with the shaded area) and the median metallicities at different stellar masses derived from the CALIFA (blue crosses; Sánchez et al. 2017) and SAMI (green diamonds; Sánchez et al. 2019) samples.

the upper panel of Figure 5, for the three galaxy samples. Field and cluster galaxies, as well as reference and stripping galaxies, are generally located on a relatively tight correlation, with no apparent signs of offset between the samples, with the exception of four among the least-massive stripping galaxies that lie well above the general relation.

Previous studies have shown that the gas-phase metallicity has a steep dependence on stellar mass for galaxies with $M_\star \leqslant 10^{10}\,M_\odot$ and then it becomes flatter at higher masses (e.g., Tremonti et al. 2004; Kewley & Ellison 2008). We fit the data with the function

$$12 + \log(\mathrm{O/H}) = \widetilde{Z} - \log\left\{\frac{1}{2}\left[\left(\frac{M_\star}{\widetilde{M}}\right)^{-\gamma} + 1\right]\right\}. \qquad (4)$$

In the log–log plane, this relation is linear for masses lower than $\widetilde{M}$ with a slope proportional to the parameter γ. At $M_\star = \widetilde{M}$, it reaches $\widetilde{Z}$ and flattens out at higher masses. We restrict the fitting to where the relation appears well defined, in the stellar mass range $9.25 \leqslant \log(M_\star/M_\odot) \leqslant 11.5$. With this choice, four low-mass galaxies, all stripping galaxies (JO45, JO149, JO181, and JW56), are excluded from the fit.

Table 2 lists the best-fit parameters obtained considering the uncertainties on the oxygen abundances. In Figure 5, we also

Table 2
Best-fit Parameters of Equation (4)

Parameter	Value	Uncertainty	
$\widetilde{Z}$	8.97	0.04	(dex)
$\log \widetilde{M}$	10.35	0.10	(dex)
γ	0.93	0.09	

show the rms around the relation (0.12 dex) in the considered mass range.[10]

In the bottom panel of Figure 5, we compare the MZR of this work with the median metallicities at different stellar masses derived by Sánchez et al. (2017, 2019) using the CALIFA and SAMI samples, respectively, and adopting the PYQZ code. Although they estimate the metallicities at the effective radius from the linear fitting of the galaxy abundance gradient (not by averaging the metallicity of the spaxels), we observe a good agreement, but at the highest and lowest masses where our MZR deviates.

Recently, Curti et al. (2020) fitted the MZR relation for $\sim$150,000 SDSS galaxies at $z > 0.027$ selected from the MPA/JHU catalog, exploiting the integrated emission fluxes inside the SDSS fiber with a 3″ diameter aperture—corresponding to a sampling of 1.6 kpc at $z = 0.027$. Curti et al. (2020) estimated the gas-phase metallicity using a combination of the calibrations developed in Curti et al. (2017) and a new series analogously determined based on nine different indexes.

We compare their MZR with the gas-phase metallicity within $0.5\,R_e$ derived with the calibrator of Curti et al. (2017) based on the O3N2 index.[11] Figure 6 shows that, overall, the fit provided by Curti et al. (2020) also well represents our data points, with an rms of the residuals of 0.07 dex. However, at $M_\star < 10^{10}\,M_\odot$, our data seem to follow a steeper trend than the relation of Curti et al. (2020). Moreover, the overabundance observed for the least-massive galaxy JO149 disappears, but it could be due to the bias of the O3N2 calibrator, as discussed in Section 3.4.

4.2. Analysis of the Residuals along the MZR

To investigate the distributions of the galaxy samples along the MZR, in Figure 7 we compute the residuals of the PYQZ gas-phase metallicity ($\Delta \log(\mathrm{O/H})$) from the best-fitting relation of Figure 5. From top to bottom, the figure shows the residuals of the reference field, reference cluster, stripping galaxies, and the overall samples of the reference and cluster galaxies, respectively. We also divide the total sample (reference+stripping galaxies) in two different equally populated stellar mass bins: $10^{9.25} \leqslant (M_*/M_\odot) < 10^{10.25}$ containing 29 galaxies and $10^{10.25} \leqslant (M_*/M_\odot) < 10^{11.5}$ containing 28 galaxies. We then compute the gas metallicity residuals of the galaxies with $M_\star < 10^{9.25}\,M_\odot$, extrapolating the MZR at low masses; therefore, these values must be taken with caution.

For galaxies in both mass bins separately, we calculate the error-weighted average value of the residuals along with its standard error. For the reference cluster galaxies, we do not

---

[10] We note that even when excluding the galaxies hosting an AGN, the fitted curve does not appreciably change.

[11] To be more consistent, we should use $\langle \mathrm{O/H} \rangle_{<0.1\,R_e}$, as our radial range is larger than 1.6 kpc (the median R_e of our sample is 4.9 kpc), but as described in Section 3.3 many galaxies lack a measurement of $\langle \mathrm{O/H} \rangle_{<0.1\,R_e}$. Figure 3 showed that $\langle \mathrm{O/H} \rangle_{<0.1\,R_e}$ and $\langle \mathrm{O/H} \rangle_{<0.5\,R_e}$ correlate well.
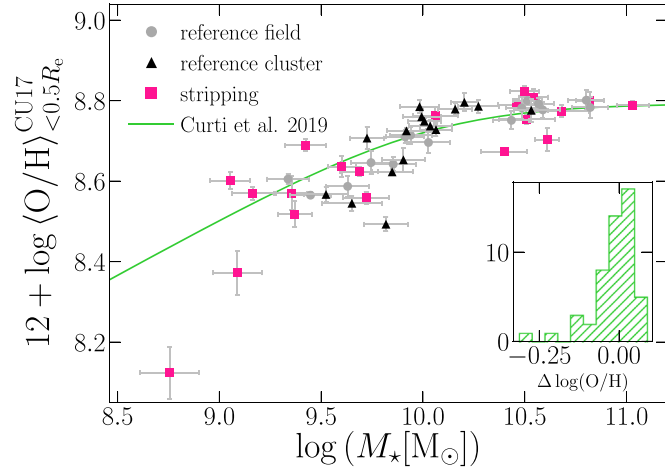
Figure 6. Relation between the galaxy stellar mass and the gas-phase metallicity within 0.5 R_e based on the O3N2 index. Symbols are as in Figure 3. The green line represents the MZR from Curti et al. (2020). The inner panel shows the histogram of the metallicity residuals of the galaxies with respect to the Curti et al. fit.

compute the mean values in the high-mass bin as there are only two objects.

The most relevant outcome that we detect occurs at $10^{9.25} \leqslant (M_*) < 10^{10.25}\,M_\odot$, where all reference field galaxies but one are located below the relation and the mean value of their residuals is lower than that of the cluster galaxies, both reference and stripping, at the $>1\sigma$ level. At high masses, the shift disappears and, in all the subsamples, the mean values of the residuals are consistent with zero.

This result appears in agreement with Maier et al. (2019a), who observed an overabundance of gas-phase metallicity in cluster galaxies with $M_\star < 10^{10.5}\,M_\odot$ compared to field galaxies of similar masses.

No strong offset emerges between the reference cluster galaxies and the stripping ones. In addition, for these galaxies, the spread of the residuals tends to decrease with increasing stellar mass, suggesting that less massive objects are more sensitive to the processes affecting the chemical evolution.

5. Discussion

In the previous section, we showed that field galaxies, cluster galaxies, and RPS galaxies follow on average a well-defined MZR, but significant deviations are also observed at low and intermediate masses between field and cluster galaxies. This means that, although the stellar mass is the parameter that mainly drives the chemical enrichment in galaxies, other physical conditions can have implications for the gas-phase metallicity evolution.

In this section, we investigate the scatter around the MZR and probe possible secondary dependencies.

5.1. The Effects of Ram Pressure Stripping

At masses $>10^{9.25}\,M_\odot$, the mean metallicity of stripping galaxies is consistent with that of the reference cluster galaxies, so the gas-stripping mechanism apparently does not determine a crucial alteration of the gas-phase metallicity at R_e. However, the RPS could entail the redistribution of gas, hence of the metals, inside the disk, producing either a reduction or an increase of the gas metallicity.
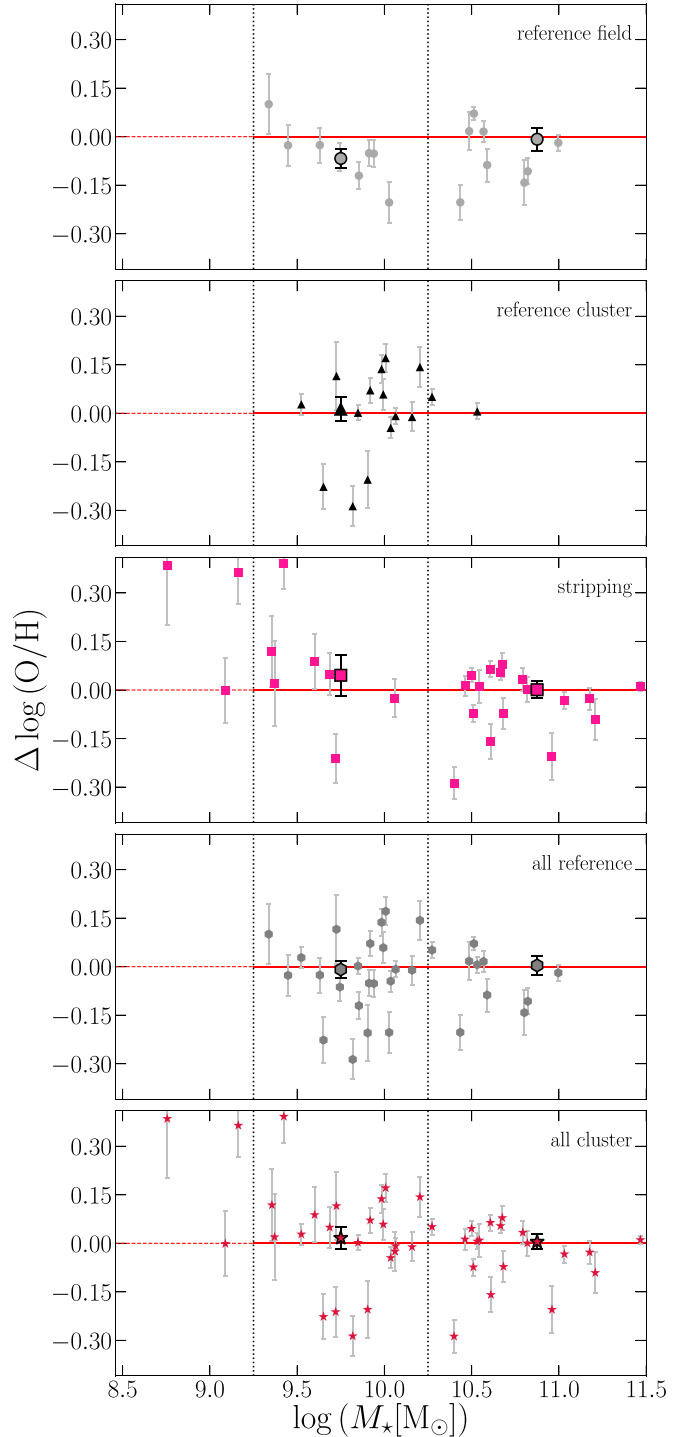

Figure 7. From the top to the bottom panels: residuals of the MZR for the reference field (gray circles), reference cluster (black triangles), stripping (pink squares), reference (reference field+cluster; dark gray hexagons), and cluster (reference cluster+stripping; red stars) galaxies. In each panel, the horizontal red line corresponds to the MZR of Figure 5, and the vertical dotted black lines are the mass separation lines at $M_\star = 10^{9.25}\,M_\odot$ and $M_\star = 10^{10.25}\,M_\odot$ dividing the samples into three mass bins. In each panel, the bigger black-edged symbols are the error-weighted average in the corresponding mass bin along with the standard errors. JW56 is not shown as its residual ($\Delta \log(O/H) = 0.73$ dex) is out of the panel limits.

On one hand, hydrodynamical simulations have found that the RPS can produce a large infall rate of gas to the inner regions, both by pushing the gas to the center and by flowing of

the galactic gas that lost angular momentum as a consequence of the interaction with the nonrotating ICM (Vollmer et al. 2001; Tonnesen & Bryan 2009; Ramos-Martínez et al. 2018). If the infalling gas was meta poor, the central metallicity, and likely that at the R_e, too, could be lower than the expectation for an undisturbed galaxy with same mass. In addition, the inward gas flow could feed the central galactic black hole and trigger its activity (Poggianti et al. 2017a); then, the consequent AGN feedback can enhance the metal ejection from the galaxy (De Rossi et al. 2017; Chisholm et al. 2018) and lead to both a reduction of the central gas-phase metallicity and an increment in the external regions.

On the other hand, simulations by Schulz & Struck (2001) have shown that RPS can also displace the gas with respect to the galaxy halo center, bringing the innermost metal-rich gas to larger radii, especially in low-mass galaxies. This possibility represents a critical issue for the $\langle O/H \rangle_{@R_e}$ estimate of the extreme stripping galaxies, whose truncation radius (the lower radius of the removed gas) is equal to or less that the R_e.

This complex scenario could be seen with the residuals of the MZR for the stripping galaxies, plotted in the middle panel of Figure 7. At stellar masses greater than $10^{9.7} M_\odot$, there are several stripping galaxies below the fitted MZR, even if their values are consistent with those of the reference sample, while at low masses, we observe stripping galaxies with higher gas-phase metallicity with respect to the relation. The Pearson correlation coefficient states that the anticorrelation with galaxy mass for stripping galaxies is significant ($r[d.f. = 25] = -0.55$, $p = 0.003$). However, the trend is no longer relevant if we exclude the four low-mass galaxies with the largest residuals above the MZR: JO162 ($\Delta \log(O/H) = 0.39$ dex), JO45 ($\Delta \log(O/H) = 0.36$ dex), JW56 ($\Delta \log(O/H) = 0.73$ dex), and JO149 ($\Delta \log(O/H) = 0.39$ dex). To better comprehend if their metallicity differences are due to the gas relocation as a consequence of the stripping, we explore the spatially resolved distribution of their gas metallicity.

Figure 8 illustrates the Hα emission and the gas-phase metallicity maps of the stripping galaxies with the largest metallicity residuals (JW56 and JO162) and those of two stripping galaxies with similar mass, but with $\langle O/H \rangle_{@R_e}$ consistent with the MZR (JO181 and JO95). In the gas-phase metallicity maps, we only plot the star-forming spaxels according to the Kauffmann et al. (2003) separation line on the N II-based BPT diagram and superimpose the R_e projected on the galaxy disk. The metallicity enhancement measured at the R_e for JW56 and JO162 is not due to the redistribution of the inner metal-rich gas outwards of the external regions, but it depends on an intrinsically overall high chemical abundance. In addition, their high $\langle O/H \rangle_{@R_e}$ values are not even due to the small size of their effective radii that might sample inner and higher metallicities; indeed, these stripping galaxies also show chemical overabundances when the mass–metallicity distribution is explored using the $\langle O/H \rangle_{disk}$ estimates. The same is valid for JO149 and JO45. One hypothesis is that this intrinsic overabundance of gas-phase metallicity might be due to a fast self-enrichment as a consequence of the SFR enhancement induced by the ram pressure process. For JO149 and JO162, this hypothesis could be true; in fact, these two galaxies have a surplus of SFR ($\Delta \log(SFR) = 0.58$ and 0.23 dex, respectively) with respect to the mass–SFR relation inferred by Vulcani et al. (2018b) using a control sample from GASP. On the other hand, JW56 and JO45 do not show the SFR boost

($\Delta \log(SFR) = 0.01$ and -0.14 dex, respectively), suggesting that for these galaxies the metallicity residuals could be connected to other physical properties.

Lastly, we have to consider that for some stripping galaxies, there are geometric effects connected to the stripping angle. The three-dimensional location of the removed gas, mainly metal poor, could be such that they overlap the galaxies along the line of sight and, thus, entails an artificial underestimation of the gas metallicity in the disk. To investigate in detail this point of view, the spatially resolved maps and the radial profiles of the gas-phase metallicity will be analyzed in a future paper (A. Franchetto et al. 2020, in preparation).

5.2. The Dependence on the Star Formation Rate

It has been shown that at a given mass, galaxies with high SFR are characterized by gas metallicity lower than those with low SFR (Lara-López et al. 2010; Mannucci et al. 2010; Hunt et al. 2012; Yates et al. 2012). We can now probe the behavior of our galaxies in this framework and verify if their gas-phase metallicity is consistent with the hypothesis of a secondary dependence on the SFR.

Figure 9 shows the gas-phase metallicity residuals of the MZR versus the SFR. The SFR values are taken from Vulcani et al. (2018b) and Gullieuszik et al. (2020), who compute and sum the SFRs of spaxels inside the galaxy boundary from the Hα flux corrected for stellar and dust absorption, excluding those spaxels classified as AGNs or LINERS by the Kewley et al. (2001) separation line in the N II-based BPT diagram, and adopting the Kennicutt (1998) relation for a Chabrier (2003) IMF. Galaxies with negative or close to zero metallicity residuals span almost the entire range of estimated SFR values, while galaxies with the largest positive residuals mainly occupy the region at low SFRs. No galaxies with high SFR are found much above the MZR. Considering the galaxies with $M^* > 10^{9.25} M_\odot$, we observe a moderate anticorrelation between the quantities, also supported by the Pearson correlation coefficient ($r[d.f. = 54] = -0.28$, $p = 0.04$). This anticorrelation is even more significant when we also include the galaxies with stellar masses below $10^{9.25} M_\odot$, for which the residuals are obtained by extrapolation of the MZR ($r[d.f. = 58] = -0.44$, $p = 0.0005$). Galaxies with the largest overabundance of gas-phase metallicity, in particular JW56, have very low total SFRs.

We have also investigated the the gas-phase metallicity residuals of the MZR versus the sSFR (plot not shown), but no statistically significant trend emerged.

Vulcani et al. (2018b) have shown that galaxies undergoing RPS have SFR values up to 0.2 dex larger than control sample galaxies of similar mass. Because this SFR surplus is likely due to the compression of the gas in the disk as a consequence of the impact with the ICM, to suitably compare the SFR of the reference and stripping samples, we scale down the SFR of the stripping galaxies and calculate again the Pearson correlation coefficient. The anticorrelation becomes more pronounced, with a higher level of significance ($r[d.f. = 58] = -0.50$, $p = 0.00004$), meaning that the metallicity scaling relation observed for the reference sample is still valid for the stripping galaxies, and the chemical evolution is driven by the same physical processes.

As discussed in the introduction, several studies have reported the existence of the mass–SFR–metallicity relations (or FMR). A direct comparison with this relation could provide further proof of the secondary dependence on the SFR.
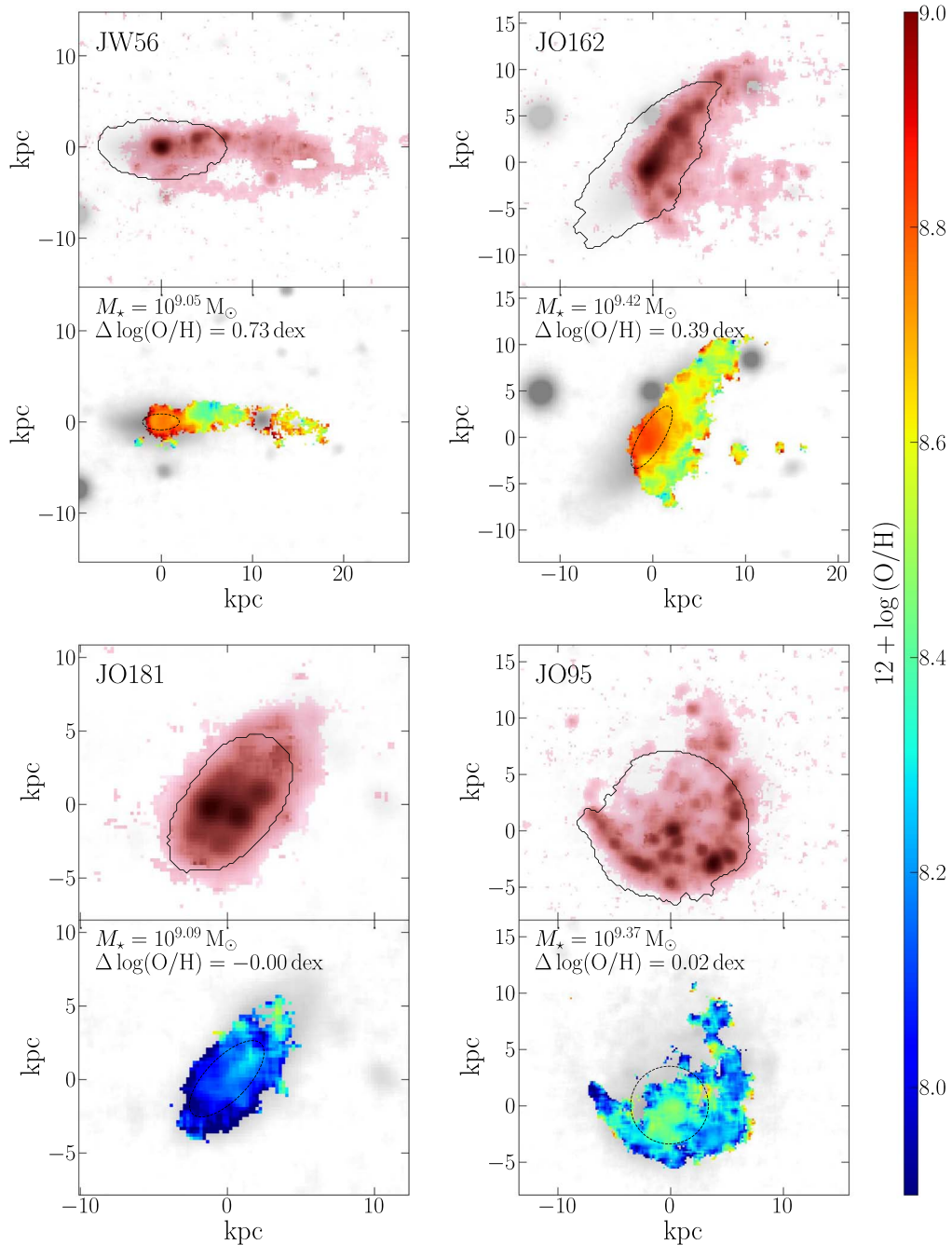
10

Figure 8. Hα emission and PYQZ gas-phase metallicity maps of the galaxies JW56, JO162, JO181, and JO95 (all stripping galaxies) superimposed on the stellar continuum underlying the Hα line (gray). JW56 and JO181 have $M_\star \approx 10^{9.07}\, M_\odot$; JO162 and JO95 have $M_\star \approx 10^{9.40}\, M_\odot$. For each galaxy, the top panel shows the Hα emission with S/N > 4 (pink) and the contour of the galaxy disk (black line); the bottom panel depicts the PYQZ gas-phase metallicity of the star-forming pixels (according to the color code) and the R_e (black dashed ellipse).

Nonetheless, this analysis is not trivial because the shape of the FMR is connected to the measurement methods of the gas metallicity and SFR, and to the selection criteria of the sample (Cresci et al. 2019).

To probe if our sample is consistent with the FMR derived by Mannucci et al. (2010), we attempt a simple emulation of their analysis and verify the distribution of our data points around the surface depicted by their FMR. Briefly, the authors used the SDSS-DR7 data set of ∼140,000 galaxies with $0.07 < z < 0.3$. SDSS spectroscopic observations were carried out with fibers of 3″ aperture, which sample a large fraction of the central galaxy region corresponding to ∼4–11 kpc depending on redshift. Mannucci et al. (2010) applied a threshold of S/N > 25 on the Hα fluxes and exclude AGN-like galaxies, adopting the diagnostics line of Kauffmann et al. (2003). The total stellar masses are taken from the MPA/JHU catalog of the SDSS-DR7 database and scaled from the Kroupa (2001) to the Chabrier (2003) IMF. The dust-corrected Hα flux inside the fiber is converted in SFR using the Kennicutt (1998) relation for a Chabrier IMF. No aperture correction is applied. The oxygen abundances are measured, adopting the calibrator described in Maiolino et al. (2008) for the N2 ([N II]6584/Hα) and R23 (([O II]3727+[O III]4958,5007)/Hβ) indexes and taking the average of the two values. Mannucci et al. first fit
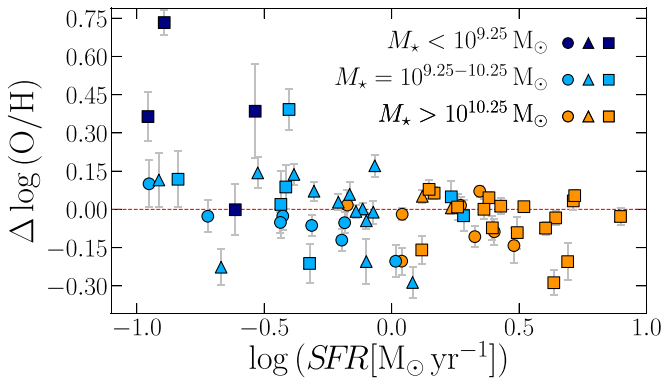
Figure 9. Residuals of the MZR vs. SFR. Circles, triangles, and squares indicate the reference field, reference cluster, and stripping galaxies, respectively. Colors refer to the galaxy stellar masses as in the legend. The horizontal red line corresponds to the MZR of Figure 5.

the mass and metallicity values with a polynomial equation in order to derive the MZR of their sample (Mannucci et al. 2010, Equation (1)); then, including the SFR values, they find the FMR (Mannucci et al. 2010, Equation (2)).

We mimic the emission-line data set of Mannucci et al. (2010), summing, for each galaxy, the flux of all the spaxels inside a circular aperture of variable size, placed in the center of the galaxy, in such a way as to sample always a diameter of 5 kpc at the redshift of the galaxies. No spaxel inside the aperture is masked before the integration. For each galaxy, the S/N of the Hα integrated flux is always greater than 25. No S/N cut is applied for the other emission lines. We exclude AGN-like galaxies by applying the diagnostic line of Kauffmann et al. (2003) and measuring the SFR using the Kennicutt (1998) relation. Finally, we compute the oxygen abundance by employing the calibration of Maiolino et al. (2008) for the N2 and R3 ([O III]5007/Hβ) indexes, and then we take the average value. We use the R3 index to substitute with the R23 one because the MUSE data do not cover the [O II]3727 line.

In Figure 10, we show the stellar-mass–SFR–metallicity space with our galaxies superimposed on the FMR surface in Mannucci et al. (2010, Equation (2)). Our sample is well distributed along the analytic relation, although it is worth making some considerations. Despite the existence of a narrow total-SFR–mass relation in the GASP sample (Vulcani et al. 2018b), the SFR values measured inside the aperture manifest a large dispersion with stellar mass; in particular, we observe some galaxies with low SFR at high masses. On the other hand, our sample does not contain galaxies with high SFR at low masses, so we are lacking data in the region where the FMR is the most sensitive to the SFR.

To quantify the scatter around the surface, we compare the gas-phase metallicity of our data points and the expected value from the FMR (Mannucci et al. 2010, Equation (2)) given the mass and the SFR. In the top panels of Figure 11, we show this comparison and the distribution of the differences. The gas-phase metallicity inferred inside the aperture is on average lower by 0.041 dex than the expected values, and the scatter amounts to 0.091 dex. The distribution is slightly asymmetric with a skewness $s = -0.21$. The shift of the metallicities toward lower values than those expected from the FMR of Mannucci et al. (2010) could be due to the fact that we adopted

the metallicity calibrator based on the R3 index instead of the R23 one, as Mannucci et al. did.

In the bottom panels of Figure 11, we compare instead our values with the expected values from the MZR curve of Mannucci et al. (2010, Equation (1)) given the stellar mass. We again note that most of the galaxies are mainly located below the considered relation. The distribution of the residuals is centered at -0.029 dex with a dispersion of 0.094 dex and is more symmetric ($s = -0.007$) than the residual distribution derived considering the FMR. At high masses, we observe a saturation of the expected values due to the flattening of the function at the high-mass end. We infer that our sample certainly follows both relations proposed by Mannucci et al. (2010); however, the scatter of our galaxies along the MZR is reduced by only 0.003 when the SFR is taken into account. We stress again that our sample does not contain galaxies with low stellar mass and high SFR. Moreover, we note that in the plane (log M, log SFR) sampled by our galaxies, the MZR and the FMR of Mannucci et al. (2010) are similar, and in fact, the metallicities of our galaxies derived using the two relations differ on average of only 0.12 dex, with a scatter of 0.04 dex.

We also obtain similar results when comparing our O3N2-based $\langle O/H \rangle_{< 0.5\,R_e}$ values, total SFRs, and galaxy stellar masses with the analytical form of the FMR presented by Curti et al. (2020, Equation (5)). The distribution of the differences along the metallicity axis between our data points and this surface almost peaks at zero (with a mean of -0.03 dex and a dispersion of 0.08 dex), although it is highly skewed ($s = -1.52$).

In conclusion, both the analysis of residuals of the gas metallicity at the R_e along the MZR using the spatially resolved data (Figure 9) and the comparison of the values inside the aperture of 5 kpc with the FMR of Mannucci et al. (2010; Figures 10 and 11) are in agreement with the possibility of a secondary dependence of the MZR on the SFR. However, this dependence is relevant only when including the very low-mass galaxies. A limitation of our analysis comes from the low number statistics and from the fact that the galaxies studied here follow a tight mass–SFR relation (Vulcani et al. 2018b): at a given mass, the galaxies span too small an SFR range to appreciate in detail the dependence on the SFR. Above $10^{9.25}\,M_\odot$, the gas metallicities of our galaxies are mainly driven by the stellar mass, and it is not necessary to introduce the SFR as third parameter to explain their distribution. On other hand, the presence of low-mass galaxies with metallicity higher than the common MZR attests to a more complex picture.

5.3. Dependence on Environment

In Figure 7, we have already observed that intermediate-mass field galaxies have on average lower gas metallicity than cluster galaxies of the same mass. Instead, at high masses, they follow a similar MZR. Reference cluster galaxies and stripping galaxies do not show a relevant offset in metallicity but are more spread along the MZR than the field galaxies. Now, we attempt to improve the analysis and investigate the relation between the gas-phase metallicity residuals and the properties of the host environment.

As previously discussed, the galaxies with the largest metallicity residuals (JO149, JW56, JO45 and JO162) are cluster galaxies with $M_\star < 10^{9.5}\,M_\odot$, in agreement with the results of Pilyugin et al. (2017), who find overabundances for
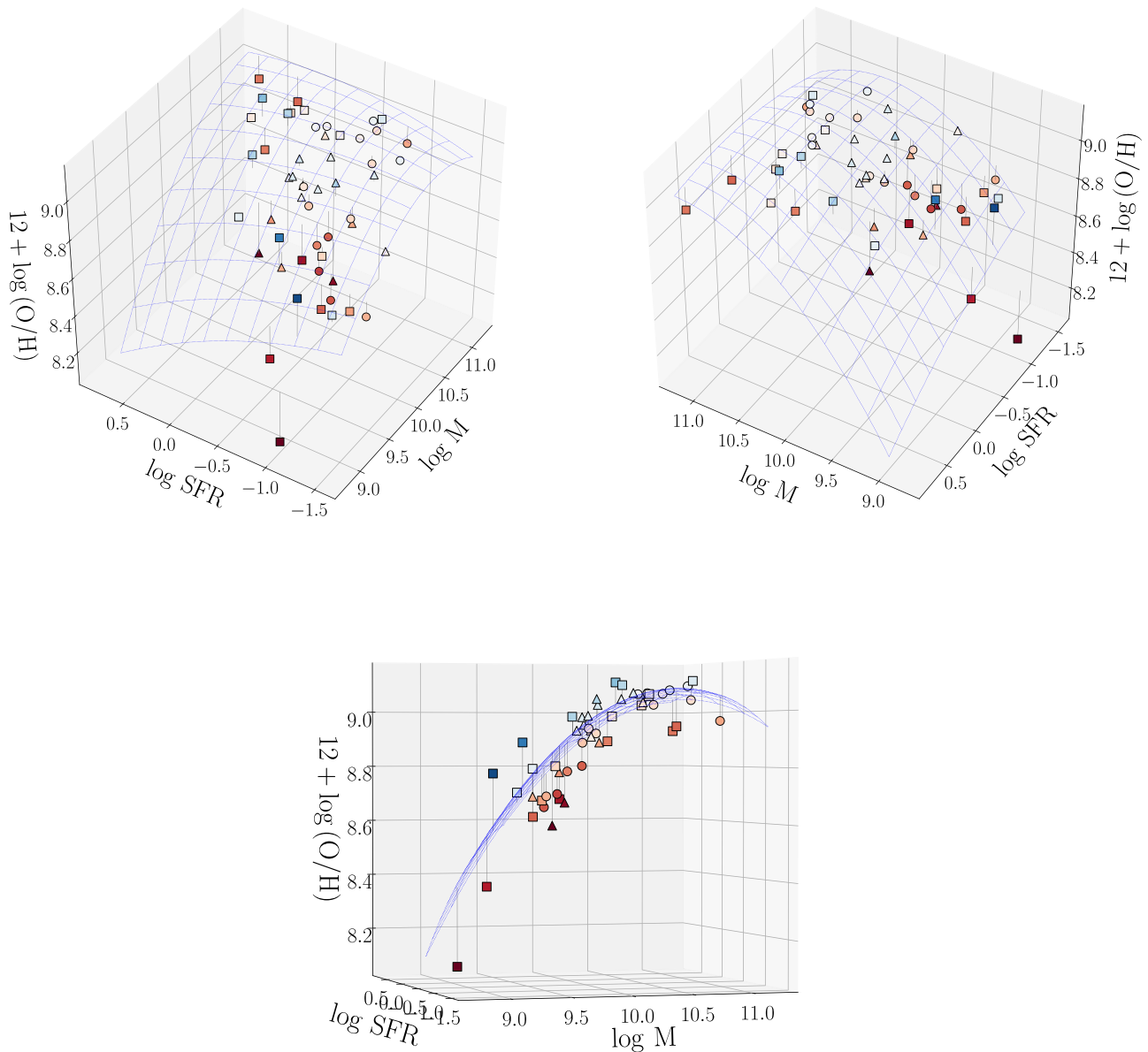
Figure 10. Three projections of the $M_\star$–SFR–metallicity space. The surface is the FMR of Mannucci et al. (2010). The circles, triangles, and squares correspond to the reference field, reference cluster, and stripping galaxies, respectively. The colors and the vertical lines indicate the metallicity distance from the surface (blue and red correspond to positive and negative differences, respectively).

low-mass galaxies $(M_\star < 10^{9.6} M_\odot)$ in the most crowded environments.

The upper panel of Figure 12 shows the distribution of the MZR residuals as a function of mass of the host halo (M_{halo}). The halo masses of the groups are taken from Paccagnella et al. (2019), while those of the clusters are from Biviano et al. (2017) and E. Munari et al. (2020, in preparation), and listed in Gullieuszik et al. (2020). No significant trends are detected, but we detect a larger scatter for the cluster galaxy sample (0.18 dex), mainly due to low-mass galaxies, than for the sample of the field galaxies (0.08 dex).

In the middle panel of Figure 12, we compare the metallicity residuals of the cluster galaxies with the projected cluster-centric distance r_p/R_{200}. Also in this case we do not observe any correlation.

For cluster galaxies, we also take into account the galaxy local density. Several studies, based on thousands of galaxies, found hints of a correlation between the gas metallicity and the local density, meaning that the local density has only a marginal role in the chemical evolution of the galaxies (Ellison et al. 2009; Peng & Maiolino 2014; Pilyugin et al. 2017).

We adopt here the projected density $\Sigma = N/A$[12] already exploited by Vulcani et al. (2012) to characterize the galaxies of the WINGS cluster survey and calculate the values for the OMEGAWINGS galaxies (B. Vulcani 2019, private communication). The lower panel of Figure 12 depicts the distribution of the residuals as a function of the local projected galaxy density. No significant trends are observed.

Finally, even when we take into account two quantities together, such as the halo mass at fixed clustercentric distance (plot not shown), no significant trend arises.

---

[12] A is the circular area that encloses the Nth nearest galaxy neighbor. Here, we adopted $N = 10$.
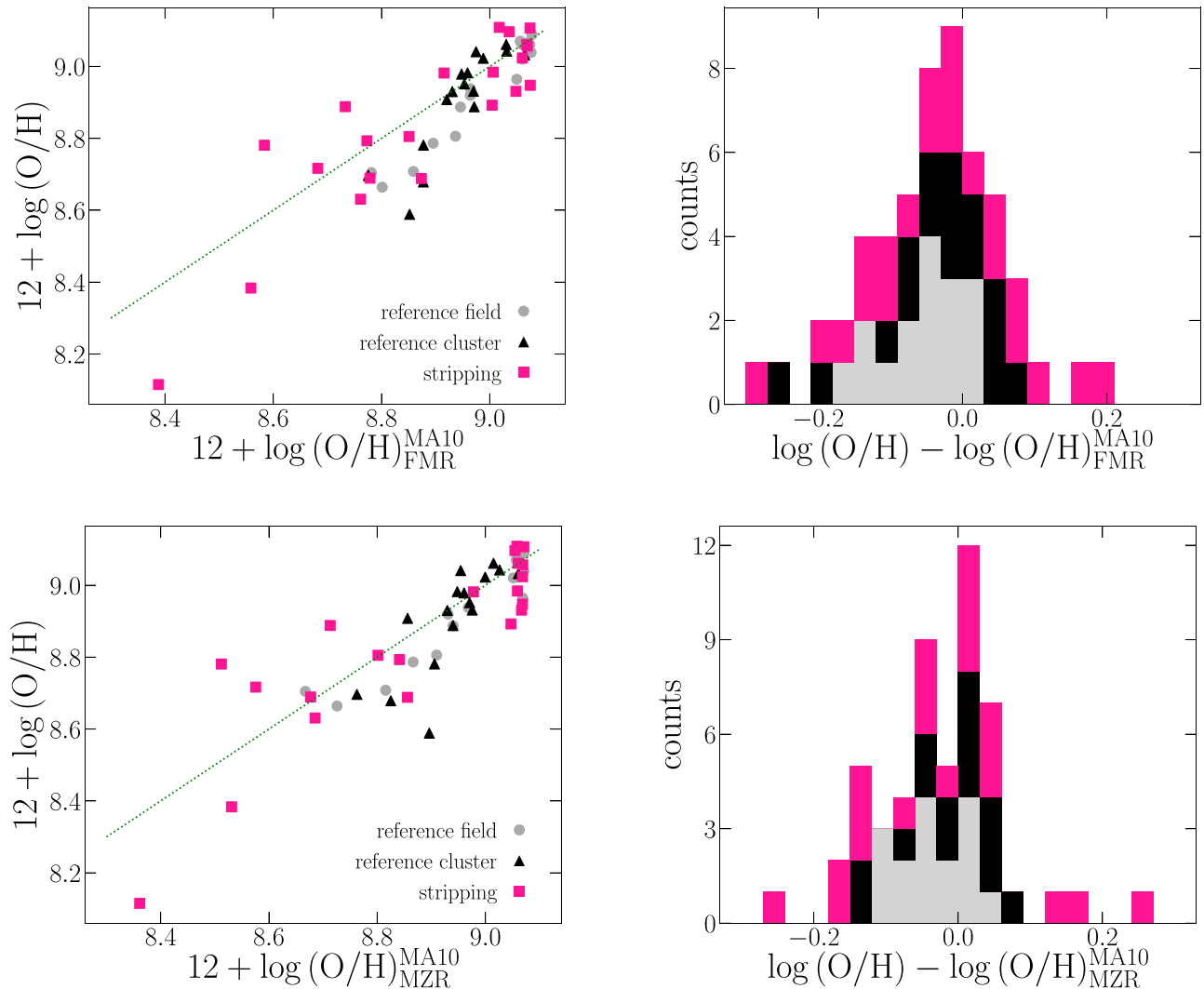
Figure 11. Upper panel: distribution of the galaxy metallicities within a diameter of 5 kpc and the expected value according to Equation (2) in Mannucci et al. (2010; on the left) and the stacked histogram of the differences (on the right). Lower panel: as in the upper panel, but considering Equation (1) in Mannucci et al. (2010). The gray circles, black triangles, and pink squares indicate the reference field, reference cluster, and stripping galaxies, respectively. The histograms follow the same color coding.

It is, however, possible that our analysis based on a relatively small sample does not have sufficient sensitivity to appreciate the environmental effects on the metal enrichment.

Nonetheless, we do observe a large scatter of the residuals for the cluster galaxies, especially the low-mass ones, suggesting that these objects could experience several processes in a dense environment, which are able to more efficiently alter the metallicity of the gas than in less dense environments. In particular, we report the case of the low-mass JW56 stripping galaxy, whose metallicity residual compared to the MZR is the largest one in the sample. This galaxy is within a highly massive galaxy cluster ($M_{halo} = 10^{14.9} M_\odot$), close to the center ($r_p/R_{200} = 0.16$), and at a high local galaxy density ($\Sigma = 10^{1.51}$ galaxies per Mpc^2). Therefore, JW56 lives in an extreme condition that not only facilitates the RPS but also could prevent the accretion of metal-poor gas and be responsible for its high metallicity.

5.4. Dependence on the Galaxy Size

Observational studies and cosmological numerical simulations observed that at a given mass, smaller galaxies are on average metal richer (Ellison et al. 2008; Sánchez Almeida & Dalla Vecchia 2018).

In Figure 13, we investigate the possible correlation with the size of the galaxies. For galaxies with $M_\star > 10^{9.25} M_\odot$, the metallicity residuals only show a mild anticorrelation with R_e (r [$d.f. = 54$] $= -0.29$, $p = 0.03$). If we include also the residuals of the lower-mass galaxies, the trend becomes more evident ($r[d.f. = 58] = -0.47$, $p = 0.0002$). In particular, we highlight that the galaxy with the largest metallicity residual (JW56) has the smallest effective radius of the sample; consequently, it is more compact than galaxies with similar mass.

We stress that the R_e of JO149 and JO95 are estimated from the mass–size relation described in the Appendix, but even if we exclude these two objects, the anticorrelation remains pronounced with the same level of significance. The R_e of the stripping galaxies could be overestimated because of the light enhancement in the external regions due to the recent star formation. Nonetheless, we do not detect significant offsets between the effective radii of the various categories (see the Appendix for details).
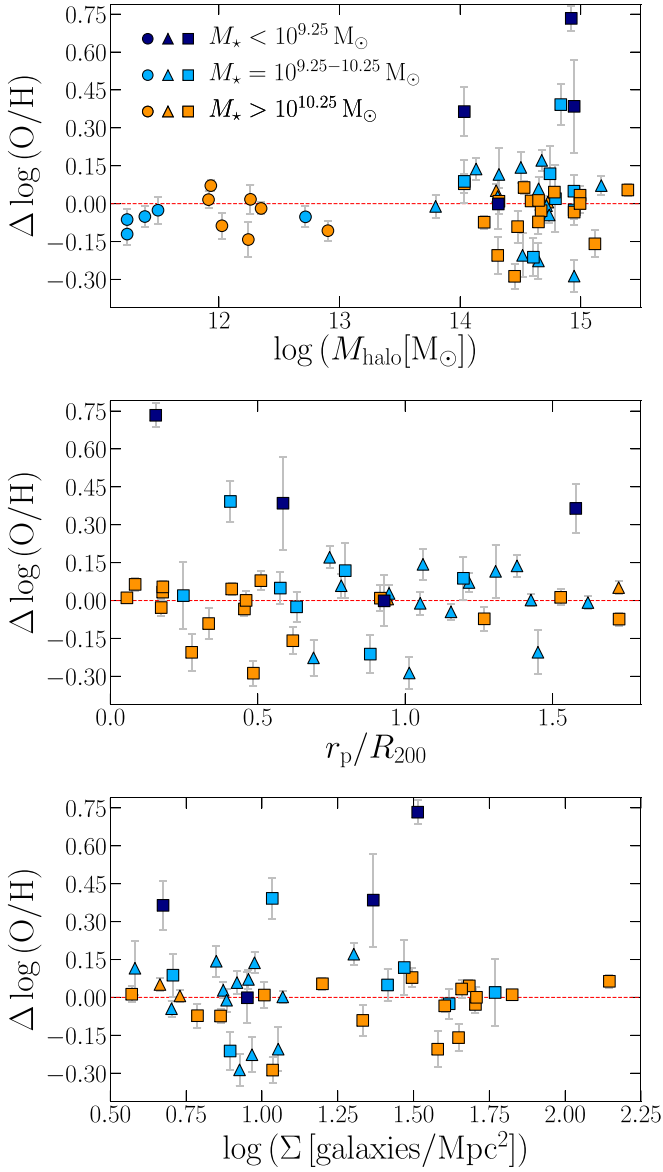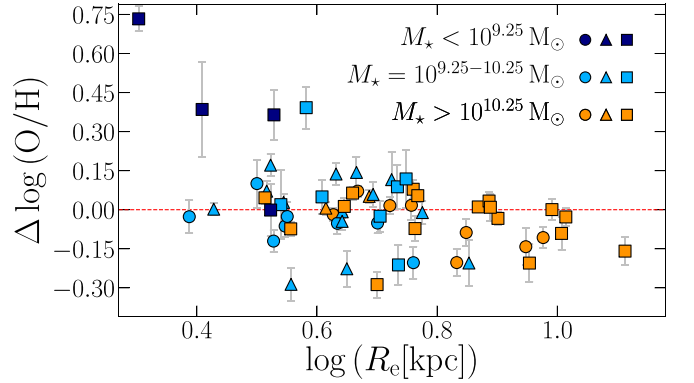
Figure 13. Residuals of MZR vs. R_e. Circles, triangles, and squares indicate the reference field, reference cluster, and stripping galaxies, respectively. Colors refer to the galaxy stellar masses as in the legend. The horizontal red line corresponds to the MZR of Figure 5.

Figure 12. Residuals of the MZR vs. M_{halo} (upper panel), vs. the projected clustercentric distance (middle panel) and vs. the projected galaxy density (lower panel). The middle and bottom panels show only the cluster galaxies. Circles, triangles, and squares indicate the reference field, reference cluster, and stripping galaxies, respectively. Colors refer to the galaxy stellar masses as in the legend. The horizontal red line corresponds to the MZR of Figure 5.

6. Summary and Conclusions

In this paper, for the first time, we studied the gas-phase metallicity relation in cluster galaxies undergoing RPS observed within the ESO MUSE GASP Program. These galaxies were selected for showing evident signs of only gas removal due to the interaction between the ICM and their ISM.

We explored the MZR of these peculiar objects in the stellar mass range $10^{8.5} \leqslant M_\star \leqslant 10^{11.5} M_\odot$ and compared it with a reference sample of galaxies, both in clusters and in the field, with no significant signs of ongoing gas-stripping processes.

To characterize the global metallicity of these galaxies, we used the PYQZ code and derived the mean gas-phase metallicity of the ionized gas at the R_e. Our relative abundances are consistent with those inferred using the empirical calibration of Curti et al. (2017) based on the O3N2 index.

Both the stripping and the reference samples follow the same well-defined MZR down to $10^{9.25} M_\odot$ with a scatter of 0.12 dex. At $M_\star < 10^{10.25} M_\odot$, the field galaxies show on average lower metallicities than the cluster galaxies, both stripping and reference, with a significance level $>1\sigma$, while at high masses the offset disappears. No differences are detected between the reference cluster galaxies and those undergoing RPS, but large scatters are observed, mainly at low masses. We detect four stripping galaxies with low masses ($<10^{9.4} M_\odot$) that have high gas metallicity with the largest differences (>0.36 dex) from the observed MZR. Their overabundance does not appear to be connected to the redistribution of the gas in the disk due to the RPS, and the importance of a fast self-enrichment as a consequence of the recent SFR enhancement by the RPS is not clear.

The scatter around the MZR can be explained by the interconnection with the physical properties of these galaxies. Indeed, results are consistent with a secondary dependence on the SFR and on the galaxy size, even if the anticorrelation between the gas-phase metallicity and these parameters is mainly driven by very low-mass galaxies. In particular, JW56, the stripping galaxy with $M_\star = 10^{9.05} M_\odot$ and the largest overabundance in the sample (0.73 dex), is more compact than galaxies with similar mass and has a very low SFR.

We did not find any correlation between the gas-phase metallicity and some environmental properties (halo mass, projected clustercentric distance, local galaxy density). However, the location of JW56, close to the center of a massive cluster, could play a role in the metal enrichment of this galaxy, preventing the accretion of metal-poor gas, in addition to fostering the RPS.

Our analysis based on the mean gas-phase metallicity at R_e did not highlight a dependence on the RPS process. Therefore, either the RPS does not alter the metal content around R_e (at least until the inner regions of the disk get stripped), or taking the mean of the metallicity values around the R_e could prevent the detection of the displacement of the gas inside the disk with respect to the galaxy center and the consequent lopsidedness of the radial gas metallicity distribution .

To investigate how the RPS works, a detailed study of the spatially resolved gas-phase metallicity (inside the disk and along the ionized gas tails) is currently ongoing and will be presented in a forthcoming paper.

Appendix
Surface Brightness Analysis

Studying the oxygen abundance at different distances from the galactic center requires knowing the structural parameters of each galaxy.

The effective radius (R_e) of the galaxies is derived by analyzing the azimuthally averaged surface brightness profile (SBP), while the position angle (PA), ellipticity (ε), and the inclination (*i*) are estimated from the disk isophotes.

The procedure we adopted exploits the *I*-band images produced by the MUSE pipeline integrating the reduced data cubes with the *I*-band filter response curve. Among the available filters entirely included in the wavelength range of MUSE, the *I*-band samples the reddest part of the spectrum. It therefore yields a smoother luminosity distribution, less affected by the youngest stars formed during recent star formation episodes and by the peaks of ionized gas emission produced by these stars. In fact, these two light sources are scattered along the galaxy disk and arise over the light of the less massive and older stars, which are more homogeneously distributed. At the redshift of the GASP galaxies, the *I* band avoids picking up the strong emission of Hα and [O III], even if the lines of [S II] always fall in this spectral range. For the same reason, the stripped gas tails appear fainter in the *I*-band images, thus preventing the SBP from being biased by the stars formed in the tails due to RPS. Furthermore, we can better observe the galactic bars that are more frequently seen at red and near-infrared wavelengths (Knapen et al. 2000). The downside is that the sky subtraction on the red part of the MUSE spectra is less effective, and we detect more sky noise than in the blue part.

We perform an isophotal analysis on the *I*-band images using the ELLIPSE task in IRAF (Jedrzejewski 1987) to extract the SBP of the galaxies. ELLIPSE fits on the image a series of elliptical isophotes such as to minimize the deviations from the real shape of the galaxy isophotes. Then, it returns the mean intensity along the ellipse, semimajor axis, PA, and ε for each one. We mask out foreground stars, nearby and background galaxies, and bad pixels before fitting the isophotes. We also mask the bright clumps on the galaxy disk that do not follow the SBP of the disk. They mainly correspond to star-forming regions and spiral arms.

Taking advantage of the wide FoV of the GASP data, we measure the radial profile of the surface brightness beyond the detectable extent of the galaxy to probe the surface brightness of the background. After having checked that the extracted SBP flattens out at large galactocentric distances, we compute the mean intensity of the unmasked pixels outside the elliptical isophotes. The inferred value is comparable with the intensity of the last isophotes and represents a residual sky level of the image. Therefore, we subtract this value from the SBP and proceed to estimate the R_e.

We derive the luminosity growth curve as the trapezoidal integral

$$L(R) = 2\pi \int_0^R I(r)(1 - \varepsilon(r))r \, dr, \qquad (A1)$$

where $I(r)$ is the SBP, $\varepsilon(r)$ is the ε profile, and r is the semimajor axis of the elliptical isophotes. By definition, the R_e is the radius that encloses half of the total luminosity L_{tot}. We approximate $L_{tot} \approx L(r_{max})$, where r_{max} corresponds to the last fitted isophote containing the whole extent of the galaxy observed in the MUSE data and compute R_e such that $L(R_e)/L_{tot} = 0.5$. In addition, in order to derive the upper and lower limits of R_e, we repeat the computation using $(I \pm \sigma)(r)$ within the integral, where σ is the error of the mean isophote intensity.

Lastly, using the isophotes that trace the galaxy disk, we calculate their mean PA and ε.

As an example, Figure A1 shows the *I*-band image of the JO49 galaxy and the SBP extracted using ELLIPSE. The magenta ellipse, traced on the image, corresponds to the outermost elliptical isophote fitted by the algorithm. We observe that the detectable extension of the galaxy is enclosed inside this isophote, also confirmed by the flattening of the SBP at the largest radius.

A.1. Mass–Size Relation

We investigate the mass–size relation of the sample, comparing the stellar mass with R_e, shown in the left panel of Figure A2. We observed a well-established correlation between the quantities, both for the reference and stripping galaxies. We explore the hypothesis that the stripping can alter the measurement of R_e due to a possible enhancement of the luminosity in the external regions of the galaxies. To examine the differences between the two samples, we fit the data with a linear regression based on a least-squares fitting method. For the reference sample we allow the slope and the intercept to vary, while for the stripping sample, we assume the same slope of the reference sample. The mass–size relations of the reference and the stripping galaxies are described by the following equations:

$$\log R_e = (0.218 \pm 0.002)\log M_\star + (-1.536 \pm 0.233)$$
$$\times \text{ (reference galaxies)}, \qquad (A2)$$

$$\log R_e = 0.218 \log M_\star + (-1.506 \pm 0.001)$$
$$\times \text{ (stripping galaxies)}, \qquad (A3)$$

with a scatter of 0.10 and 0.13 dex, respectively. The difference between the two fits is ~0.030 dex. Differences are better seen in the right panel of Figure A2, which shows the distribution of the difference between the R_e of each galaxy and the value derived from the reference sample fit given the galaxy mass. Although there is a small tail toward higher values of R_e for the
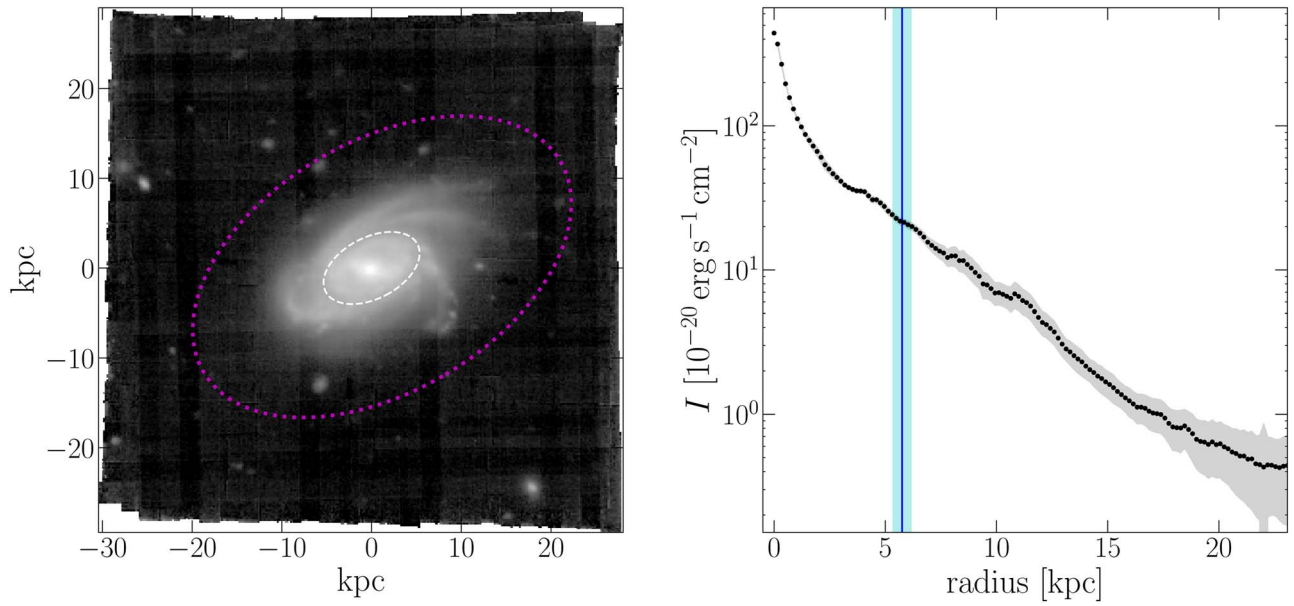
Figure A1. Left panel: *I*-band image of the JO49 galaxy. The white inner ellipse indicates the R_e of the galaxies according to the mean ε and the mean PA of the disk. The magenta ellipse corresponds to the outermost elliptical isophote fitted by the ELLIPSE algorithm. Right panel: radial profile of the surface brightness along with the rms errors of JO49 extracted by ELLIPSE. The vertical blue line and the cyan area indicate the inferred R_e and the corresponding error.
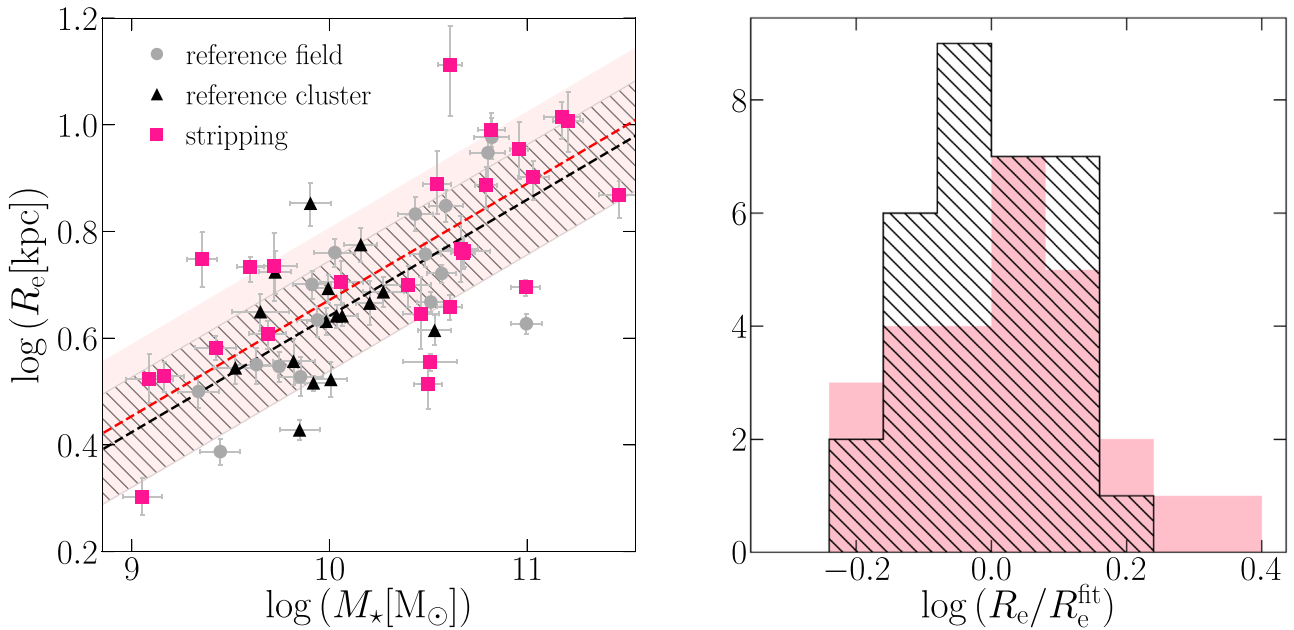

Figure A2. Left panel: relation between the galaxy stellar mass and the R_e. The gray circles, black triangles, and pink squares indicate the reference field, reference cluster, and stripping galaxies, respectively. The black dotted line and the dashed gray area show the best linear fit and the rms error for the reference sample. The red dotted line and the pink area show the best linear fit and the rms error for the stripping galaxy sample, adopting the same slope as the reference sample fit. Right panel: distribution of the differences between the estimated effective radii and the expected values according to the best fit of the reference sample, given the stellar mass. The black dashed area corresponds to the reference sample, the pink area refers to the stripping galaxy sample.

stripping galaxies, the KS test cannot reject the hypothesis that the two distributions are drawn from the same parent distribution (*p*-value ~ 0.28).

ORCID iDs

Andrea Franchetto ● https://orcid.org/0000-0001-9575-331X
Benedetta Vulcani ● https://orcid.org/0000-0003-0980-1499
Bianca M. Poggianti ● https://orcid.org/0000-0001-8751-8360
Marco Gullieuszik ● https://orcid.org/0000-0002-7296-9780
Matilde Mingozzi ● https://orcid.org/0000-0003-2589-762X
Alessia Moretti ● https://orcid.org/0000-0002-1688-482X
Neven Tomičić ● https://orcid.org/0000-0002-8238-9210
Jacopo Fritz ● https://orcid.org/0000-0002-7042-1965
Daniela Bettoni ● https://orcid.org/0000-0002-4158-6496
Yara L. Jaffé ● https://orcid.org/0000-0003-2150-1130

References

Bacon, R., Accardo, M., Adjali, L., et al. 2010, Proc. SPIE, 7735, 773508
Baldwin, J. A., Phillips, M. M., & Terlevich, R. 1981, PASP, 93, 5

Barrera-Ballesteros, J. K., Sánchez, S. F., Heckman, T., Blanc, G. A. & The MaNGA Team 2017, ApJ, 844, 80
Bellhouse, C., Jaffé, Y. L., Hau, G. K. T., et al. 2017, ApJ, 844, 49
Bellhouse, C., Jaffé, Y. L., McGee, S. L., et al. 2019, MNRAS, 485, 1157
Biviano, A., Moretti, A., Paccagnella, A., et al. 2017, A&A, 607, A81
Blanc, G. A., Kewley, L., Vogt, F. P. A., & Dopita, M. A. 2015, ApJ, 798, 99
Blanc, G. A., Lu, Y., Benson, A., Katsianis, A., & Barraza, M. 2019, ApJ, 877, 6
Boselli, A., & Gavazzi, G. 2006, PASP, 118, 517
Calvi, R., Poggianti, B. M., & Vulcani, B. 2011, MNRAS, 416, 727
Cardelli, J. A., Clayton, G. C., & Mathis, J. S. 1989, ApJ, 345, 245
Chabrier, G. 2003, PASP, 115, 763
Chisholm, J., Tremonti, C., & Leitherer, C. 2018, MNRAS, 481, 1690
Cooper, M. C., Tremonti, C., Newman, J. A., & Zabludoff, A. I. 2008, MNRAS, 390, 245
Cowie, L. L., & Songaila, A. 1977, Natur, 266, 501
Cresci, G., Mannucci, F., & Curti, M. 2019, A&A, 627, A42
Curti, M., Cresci, G., Mannucci, F., et al. 2017, MNRAS, 465, 1384
Curti, M., Mannucci, F., Cresci, G., & Maiolino, R. 2020, MNRAS, 491, 944
De Masi, C., Matteucci, F., & Vincenzo, F. 2018, MNRAS, 474, 5259
De Rossi, M. E., Bower, R. G., Font, A. S., Schaye, J., & Theuns, T. 2017, MNRAS, 472, 3354
De Rossi, M. E., Theuns, T., Font, A. S., & McCarthy, I. G. 2016, BAAA, 58, 24
Dopita, M. A., Sutherland, R. S., Nicholls, D. C., Kewley, L. J., & Vogt, F. P. A. 2013, ApJS, 208, 10
Ellison, S. L., Patton, D. R., Simard, L., & McConnachie, A. W. 2008, AJ, 135, 1877
Ellison, S. L., Simard, L., Cowan, N. B., et al. 2009, MNRAS, 396, 1257
Fasano, G., Marmo, C., Varela, J., et al. 2006, A&A, 445, 805
Fossati, M., Fumagalli, M., Boselli, A., et al. 2016, MNRAS, 455, 2028
Fritz, J., Moretti, A., Gullieuszik, M., et al. 2017, ApJ, 848, 132
Garnett, D. R. 2002, ApJ, 581, 1019
Giovanelli, R., Haynes, M. P., Salzer, J. J., et al. 1994, AJ, 107, 2036
Gullieuszik, M., Poggianti, B., Fasano, G., et al. 2015, A&A, 581, A41
Gullieuszik, M., Poggianti, B. M., McGee, S. L., et al. 2020, ApJ, submitted
Gullieuszik, M., Poggianti, B. M., Moretti, A., et al. 2017, ApJ, 846, 27
Gunn, J. E., Gott, J., & Richard, I. 1972, ApJ, 176, 1
Haffner, L. M., Dettmar, R. J., Beckman, J. E., et al. 2009, RvMP, 81, 969
Hirschauer, A. S., Salzer, J. J., Janowiecki, S., & Wegner, G. A. 2018, AJ, 155, 82
Hunt, L., Magrini, L., Galli, D., et al. 2012, MNRAS, 427, 906
Jaffé, Y. L., Poggianti, B. M., Moretti, A., et al. 2018, MNRAS, 476, 4753
Jedrzejewski, R. I. 1987, MNRAS, 226, 747
Kauffmann, G., Heckman, T. M., Tremonti, C., et al. 2003, MNRAS, 346, 1055
Kennicutt, R. C. J. 1998, ApJ, 498, 541
Kewley, L. J., Dopita, M. A., Sutherland, R. S., Heisler, C. A., & Trevena, J. 2001, ApJ, 556, 121
Kewley, L. J., & Ellison, S. L. 2008, ApJ, 681, 1183
Knapen, J. H., Shlosman, I., & Peletier, R. F. 2000, ApJ, 529, 93

Kroupa, P. 2001, MNRAS, 322, 231
Krühler, T., Kuncarayakti, H., Schady, P., et al. 2017, A&A, 602, A85
Lara-López, M. A., Cepa, J., Bongiovanni, A., et al. 2010, A&A, 521, L53
Larson, R. B., Tinsley, B. M., & Caldwell, C. N. 1980, ApJ, 237, 692
Maier, C., Hayashi, M., Ziegler, B. L., & Kodama, T. 2019a, A&A, 626, A14
Maier, C., Ziegler, B. L., Haines, C. P., & Smith, G. P. 2019b, A&A, 621, A131
Maiolino, R., & Mannucci, F. 2019, A&ARv, 27, 3
Maiolino, R., Nagao, T., Grazian, A., et al. 2008, A&A, 488, 463
Mannucci, F., Cresci, G., Maiolino, R., Marconi, A., & Gnerucci, A. 2010, MNRAS, 408, 2115
Mingozzi, M., Belfiore, F., Cresci, G., et al. 2020, A&A, 636, 42
Moretti, A., Poggianti, B. M., Gullieuszik, M., et al. 2018, MNRAS, 475, 4055
Navarro, J. F., Frenk, C. S., & White, S. D. M. 1996, ApJ, 462, 563
Paccagnella, A., Vulcani, B., Poggianti, B. M., et al. 2019, MNRAS, 482, 881
Peng, Y.-j., & Maiolino, R. 2014, MNRAS, 438, 262
Pilyugin, L. S., Grebel, E. K., Zinchenko, I. A., Nefedyev, Y. A., & Mattsson, L. 2017, MNRAS, 465, 1358
Poggianti, B. M., Gullieuszik, M., Tonnesen, S., et al. 2019, MNRAS, 482, 4466
Poggianti, B. M., Jaffé, Y. L., Moretti, A., et al. 2017a, Natur, 548, 304
Poggianti, B. M., Moretti, A., Gullieuszik, M., et al. 2017b, ApJ, 844, 48
Radovich, M., Poggianti, B., Jaffé, Y. L., et al. 2019, MNRAS, 486, 486
Ramos-Martínez, M., Gómez, G. C., & Pérez-Villegas, Á. 2018, MNRAS, 476, 3781
Rodríguez-Baras, M., Díaz, A. I., & Rosales-Ortega, F. F. 2019, A&A, 631, A23
Sánchez Almeida, J., & Dalla Vecchia, C. 2018, ApJ, 859, 109
Sánchez, S. F., Barrera-Ballesteros, J. K., López-Cobá, C., et al. 2019, MNRAS, 484, 3042
Sánchez, S. F., Barrera-Ballesteros, J. K., Sánchez-Menguiano, L., et al. 2017, MNRAS, 469, 2121
Sánchez, S. F., Rosales-Ortega, F. F., Jungwiert, B., et al. 2013, A&A, 554, A58
Sanders, R. L., Shapley, A. E., Zhang, K., & Yan, R. 2017, ApJ, 850, 136
Schulz, S., & Struck, C. 2001, MNRAS, 328, 185
Sharp, R. G., & Bland-Hawthorn, J. 2010, ApJ, 711, 818
Sutherland, R. S., & Dopita, M. A. 1993, ApJS, 88, 253
Tonnesen, S., & Bryan, G. L. 2009, ApJ, 694, 789
Tremonti, C. A., Heckman, T. M., Kauffmann, G., et al. 2004, ApJ, 613, 898
Vogt, F. P. A., Dopita, M. A., Borthakur, S., et al. 2015, MNRAS, 450, 2593
Vollmer, B., Cayatte, V., Balkowski, C., & Duschl, W. J. 2001, ApJ, 561, 708
Vulcani, B., Poggianti, B. M., Fasano, G., et al. 2012, MNRAS, 420, 1481
Vulcani, B., Poggianti, B. M., Gullieuszik, M., et al. 2018a, ApJL, 866, L25
Vulcani, B., Poggianti, B. M., Jaffé, Y. L., et al. 2018b, MNRAS, 480, 3152
Vulcani, B., Poggianti, B. M., Moretti, A., et al. 2018c, ApJ, 852, 94
Vulcani, B., Poggianti, B. M., Moretti, A., et al. 2019, MNRAS, 487, 2278
Wu, P.-F., Zahid, H. J., Hwang, H. S., & Geller, M. J. 2017, MNRAS, 468, 1881
Yates, R. M., Kauffmann, G., & Guo, Q. 2012, MNRAS, 422, 215
Zhang, K., Yan, R., Bundy, K., et al. 2017, MNRAS, 466, 3217